# Fluorination and its Effects on Electrocatalysts for Low-Temperature Fuel Cells

Marian Chatenet, Sandrine Berthon-Fabry, Yasser Ahmad, K. Guérin, Marie Colin, Hani Farhat, Lawrence Frezet, Gaixia Zhang, Marc Dubois

# Fluorination and its effects on electrocatalysts for low-temperature fuel cells

*Marian Chatenet[1], Sandrine Berthon-Fabry[2], Yasser Ahmad[3], Katia Guérin[2,4], Marie Colin[4], Hani Farhat[4], Lawrence Frezet[4], Gaixia Zhang[5], Marc Dubois[4,]**

[1] Univ. Grenoble Alpes, Univ. Savoie Mont Blanc, CNRS, Grenoble INP (Institute of Engineering and Management Univ. Grenoble Alpes), LEPMI, 38000 Grenoble, France

[2] MINES ParisTech, PSL University, Centre for processes, renewable energy and energy systems (PERSEE), CS 10207, 06904 Sophia Antipolis Cedex, France

[3] Fahad Bin Sultan University, College of Science and Humanities, Department of Natural Sciences, Tabuk, 71454, Kingdom of Saudi Arabia.

[4] Université Clermont Auvergne, Clermont Auvergne INP, CNRS, Institut de Chimie de Clermont-Ferrand (ICCF), F-63000 Clermont–Ferrand, France.

[5] Department of Electrical Engineering, École de Technologie Supérieure (ÉTS), Montréal, Québec H3C 1K3, Canada

E-mail: marc.dubois@uca.fr

Keywords: Electocatalyst, fuel cell, carbonaceous materials, fluorination, doping

***Abstract***

The benefits of covalent grafting of fluorine atoms onto carbonaceous materials are described for the design of new electrocatalysts for low-temperature fuel cells. In order to obtain the best results, the fluorination conditions must be carefully chosen according to the physicochemical properties of the starting materials (specific surface area, pore size distribution, crystallinity, doping). By describing the main fluorination routes, the article aims to help in the choice of efficient treatment conditions. The effects of fluorination on the performance of the platinum group metal (PGM)-based catalyst and the non-PGM-based electrocatalyst are discussed.

Finally, future research prospects and technical challenges of fluorination for fuel cells are proposed.

## 1. Introduction

Hydrogen Fuel Cells ($H_2$ FCs, $H_2$/air FCs, or $H_2/O_2$ FCs for short) are electrochemical power generators that combine hydrogen and oxygen (from air) to produce electricity, with water as the only by-product. Thus, $H_2$ fuel cells are considered one of the most promising and attractive candidates for a wide variety of power applications ranging from portable and transportation to large-scale stationary power systems for buildings and distributed generation. The wide commercialization of this sustainable energy technology will greatly help to tackle climate change by reducing greenhouse and toxic gas emissions.

Because of their advantages (zero-emission, high efficiency, and broad applications), $H_2$/air FCs have attracted considerable interest from industry and governments worldwide. Particularly, the low-temperature fuel cells (operating temperature usually is lower than 100 °C, more often at 80 °C), such as the polymer electrolyte fuel cells (PEFCs) including proton exchange membrane fuel cells (PEMFCs) and anion exchange membrane fuel cells (AEMFCs), have attracted intensive attention due to their easy startup and high power density, especially for use in transportation applications [1-2]. For their working principles (as shown in Scheme 1), basically, a single fuel cell consists of a membrane sandwiched by two electrodes, with catalysts on both electrodes to promote the chemical reactions. Taking the PEMFC as an example, at the anode side, $H_2$ is fed in and split into protons and electrons with the help of the catalysts. The protons are conducted through the membrane to the cathode side, while the electrons travel through an external circuit, supplying electricity. At the cathode side, $O_2$ comes in and reacts with the protons and electrons to form water and heat. In contrast to a PEMFC, an AEMFC works with a membrane that transports $OH^-$ ions from the cathode to the anode during power generation, and at the anode, the $OH^-$ ions react with $H_2$ gas to form water. Many single fuel cell units are usually combined to form a fuel cell stack for practical applications. So far, the widespread commercialization of low-temperature fuel cells is still hampered by their high cost, especially due to the use of rare and expensive platinum-based electrocatalysts, which account for 40% of the FC stack cost but are mainly required to facilitate the slow Oxygen Reduction Reaction (ORR) at the FC cathode.

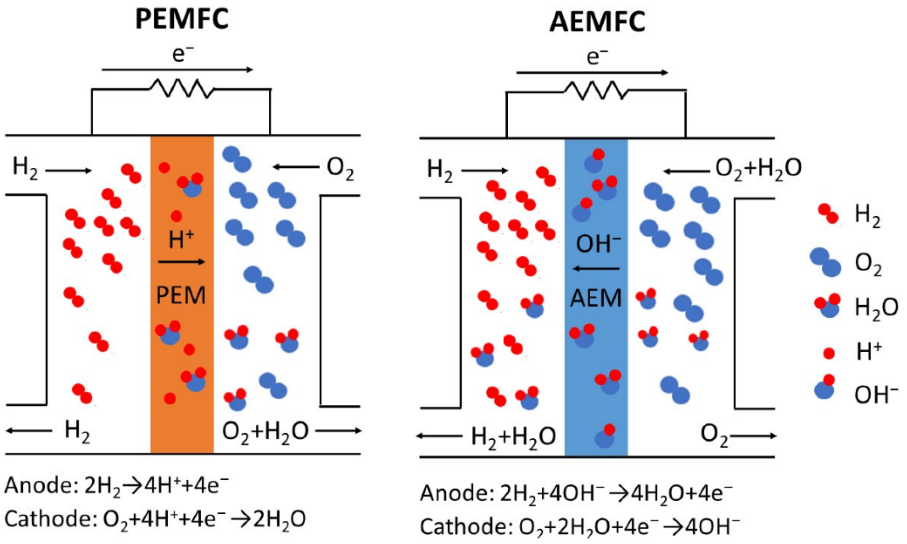


**Scheme 1.** Working principles of (a) PEMFC and (b) AEMFC, and their relevant anode and cathode reactions. Reproduced with permission from [3-4] Copyright 2021, MDPI.

Currently, two lines of research and development are being pursued regarding carbon-based electrocatalysts: the platinum group metal (PGM)-based catalyst and the PGM-free electrocatalyst [5-7]. The first axis concerns PEFCs with precious metal-based electrocatalysts. Platinum (Pt) is known to be the most active one, especially for ORR, which is the limiting reaction occurring at the cathode with slow kinetics (See Part 3). To limit the amount used, Pt alloys (3d transition metal or rare earth elements) are also studied. For reasons of cost limitation and to avoid the use of critical raw materials, the second axis concerns the development of non-PGM-based electrocatalyst materials as an alternative (see part 4) [8-10]. A lot of research has been done and M-N-C catalysts with M=Fe have shown strong ORR activity in acidic media. The half-wave potential measured by a rotating disk electrode (RDE) approaches that of Pt/C but their efficiency is limited in $H_2$/air PEFCs, due to the lower mass-transport properties induced by the high catalyst loading needed to achieve sufficient electrode activity (leading a thick layer of 70−100 µm for loading of 4 mg $cm^{-2}$ (vs 10-15 µm for Pt/C ) [9, 11]).

With the aim to develop low-cost, highly active and stable hydrogen/air, two routes consist of the enhancements of the electrode activities and stability but also of the electrolyte/electrode interface stability. Both routes concern Platinum-Group-Metal (PGM) and non-Platinum-Group-Metal (non-PGM) catalysts.

The non-PGM catalysts [8-10] exemplify well the need for stability. Although much cheaper than the PGM catalysts, most of them face the problem of their short shelf-life. Enhancing the catalyst shelf-life would efficiently/equally enlarge the lifecycle of their use in fuel cells. The demetallation of FeNx active sites (e.g., $FeN_4$) in Fe/N/C catalyst (which have much higher

activity than the metal-free $CN_x$ sites [12] including carbon-nitrogen sites, carbon edge, and defects) is at the origin of the fast decay of the catalyst activity [13]. An alternate explanation to the current decay of Fe/N/C is the attack by $H_2O_2$ and/or free radicals (intermediate in $O_2$ reduction) [14]. Investigations must focus on processes that would both prevent the demetallation of $FeN_x$ sites and stabilize the carbon support against any oxidation/electro-oxidation. One notes that this last strategy would be also beneficial for PGM catalyst. Inspired by the stabilization of the ionomers in fuel cells (like Nafion, Aquivion, etc.) through a perfluorination of the previously used non-fluorinated ionomers, a promising route emerges: rational fluorination of Fe/N/C catalyst, or of the high surface area carbon that supports PGM-based nanoparticles, for highly active and stable $H_2$ fuel cells. On the one hand, the strong bond between F and C makes it durable and resistant to chemical attack (*e.g.*, $H_2O_2$, free radicals) and, on the other hand, the stable carbon support by fluorination would also alleviate the demetallation of $FeN_x$ sites from the carbon atoms around. In that latter case, active centers are generated and strengthening of the force between oxygen and carbon occurs because of the polarization of carbon adjacent to highly electronegative fluorine [15]. Several examples highlight the benefits allowed by the presence of fluorine atoms because of the large difference between the electronegativities of fluorine and carbon elements. Both the electrochemical reaction property and stability for full water splitting and supercapacitor are improved via a strategy of N and F co-doping for graphene quantum dots [16]. N and F co-doping of reduced graphene oxide allows ORR stability to be enhanced [17]. Numerous other examples will be discussed thereafter.

This review will summarize and discuss the latest progress and advances in employing fluorination techniques for low-temperature fuel cell applications. Especially, it will focus on the discussion of why fluorination is relevant and how it can be carried out to maintain both an adequate pore size distribution and a conductive state for electrochemical processes, as well as eventually the hetero-dopings (e.g., F, N, S, and P) in the catalysts that are necessary for the high ORR activity. So far, some review articles have addressed the fluorination effects on the properties and degradation of liquid ionomers and polymer membranes in fuel cells such as i) ionic conductivity, ii) chemical, mechanical, thermal, oxidative, and hydrolytic stabilities, iii) the capability for fabrication into membrane electrode assemblies (MEAs), iv) the role of fluorinated polymers in the water management, etc. [18-21]. However, the fluorination effects on the material properties and the fuel cell performance and stability of the catalysts and the catalyst layers have rarely been comprehensively discussed, which is exactly what this review paper strives to address. Additionally, the versatility of the gas/solid fluorination for such an

aim will be highlighted. This heterogenous reaction with elemental fluorine is preferred because it can easily allow treatment at the industrial scale. Further, the comprehensive investigation of the bonding (such as C-F) in the fluorinated materials through various characterizations, including Fourier-transform infrared spectroscopy (FTIR), nuclear magnetic resonance (NMR), X-ray photoelectron spectroscopy (XPS), electron paramagnetic resonance (EPR), X-ray absorption near edge structure (XANES), will be discussed. In the two last sections, the effects of fluorination on both PGM and non-PGM catalysts will be discussed, with special emphasis on the apparent activity and durability of the materials. Finally, future research perspectives and technical challenges of fluorination for fuel cells are proposed.

## 2. Fluorination of porous carbonaceous materials

### 2.1. Methods and expected benefits

Fluorination is proven to be an effective route to provide high-value functions to materials either on their surface or in the bulk. Because of the particular properties of fluorine element, *i.e.,* high electronegativity (4.1 versus 3.5 and 2.8 for O and Cl, respectively), low polarizability ($0.81.10^{24}$ $cm^3$ for F, $3.10^{24}$ $cm^3$ for O), low van der Waals radius (0.135 nm), low dissociation energy for elemental fluorine $F_2$ (153 $kJ.mol^{-1}$), it stands as a successful candidate to tailor novel materials' properties. Its ability to form stable chemical bonding with carbon with a bonding energy of 513 $kJ.mol^{-1}$ for C-F bond and the possible tailoring of the porosity of the porous carbonaceous material are also noticeable [22]. Fluorination of porous (nano)carbons has witnessed tremendous development in the last few decades owing to the interesting properties induced by the highly-reactive fluorine atom [23-25]. In fact, besides improving wettability and chemical stability, fluorination is efficient to modulate the electrical properties of the carbonaceous matrix. As a representative example, the band gap and transport properties of graphene may be modulated according to the fluorine content and consequently the ratio of the carbon atoms with $sp^2$ (non-fluorinated) and $sp^3$ hybridization (fluorinated) [26-28].

Covalent grafting of fluorine atoms, however, is a remaining challenge, especially with low graphitized porous materials. Unsuccessful fluorination is generally ascribed to the chemical decomposition of the carbonaceous material caused by the over-reactivity of fluorine atoms, which hinders the covalent functionalization of the carbon with fluorine atoms. Yet, overcoming this challenge would be a great opportunity to achieve both well-dispersed C-F bonds and perfectly-controlled porosity. For all these reasons, chemists should be able to control the fluorination reaction using mild conditions.

Heterogenous gas/solid process occurring in the fluorine-containing atmosphere appears as a scalable route. The fluorine content**,** *i.e.,* atomic F/C ratio**,** and the C-F bonding (ionic, semi-ionic or covalent) are modulated by the fluorination conditions such as the pressure, the fluorination temperature, the duration and the composition of the gaseous species, in particular, HF or other inorganic fluorides that may be present and act as catalysts [4, 29-30]. Moreover, different fluorination parameters and fluorinating species (molecular or atomic fluorine) may be used to favor fluorine diffusion into the carbonaceous lattice. However, covalent grafting of fluorine atoms can compete with the decomposition of the carbonaceous lattice. Thereby, a minute control of the fluorination conditions must be achieved as a function of the characteristics of the starting carbonaceous material (such as the graphitization degree, $sp^2$ ratio, presence of hetero-element such as O, H and N, and specific surface area) allowing to minimize the number of structural defects such as $CF_2$ and $CF_3$ and dangling bonds that may influence the performances of the materials [29, 31].

The fluorination conditions depend on the state of structural organization of the starting materials. The higher the structural order, the higher the fluorination temperature. Graphite can be fluorinated with pure $F_2$ gas at temperatures higher than 350°C and up to 650°C. On the contrary, amorphous carbons may be fluorinated with diluted elemental fluorine at room temperature. For dual carbonaceous materials with regions of different crystalline orders, fluorination focuses on amorphous parts. The fluorination of carbon nanodiscs perfectly exemplifies this behavior, which results in the decomposition of the amorphous carbons [32].

**Direct fluorination using molecular fluorine**

When performed either in dynamic mode (with a flux of gases within the reactor connected to a soda lime trap) or in static mode (a defined amount of reactive gas is injected in a closed reactor), direct fluorination remains the most common route to prepare fluorinated carbons [33-34]. Both the reactivity and the exothermicity of the reaction must be controlled to avoid the collapse of the porous structure and huge decomposition when materials with a high specific surface area are under consideration. The continuous flow of $F_2$ in the dynamic mode renews the reactive species onto the surface of the target and favors the decomposition and/or formation of defects[35-37]. The term of over-fluorination is then used in comparison with perfluorination, *i.e.,* when all the carbon atoms are fluorinated in a $CF_1$ composition for carbonaceous materials (-$[CF_2$-$CF_2]_n$- for the case of polyethylene -$[CH_2$-$CH_2]_n$-).

To avoid over-fluorination, by reducing the oxidizing potential of $F_2$, operating at room temperature is not enough and mixtures of fluorine with an inert gas, most commonly nitrogen,

helium or argon, must be used. Depending on the intended F/C ratio and the starting material, fluorine concentration in the gaseous mixture may vary from 1 to 100% range and the partial pressure of fluorine can range between 0.005 and 1 bar.

**Indirect fluorination using fluorinating reagents**

Indirect fluorination involves fluorine atoms and/or molecules, *i.e.,* atomic F$^{\bullet}$ and/or $F_2$, which are gradually generated by the thermal decomposition of a fluorine-containing solid such as $TbF_4$ and $XeF_2$. This way allows adjusting the concentration of the fluorine released (atomic F$^{\bullet}$ or molecular $F_2$) and thus can perfectly control the carbon-fluorine reactivity and hence the F/C ratio of the synthesized material, *e.g.,* carbon aerogels [4], porous carbons [38], nanofibers [34, 39-40], nanodiscs [32, 40-41]. Because the diffusions of atomic and elemental fluorine are different, the fluorination mechanisms differ between these two species. The dispersions in sub-fluorinated carbons (F/C lower than 1) are more homogenous with atomic F$^{\bullet}$ [33, 39-40] and the structural type formed may be different; $(C_2F)_n$ type is not formed because $(CF)_n$ is exclusively achieved with atomic F$^{\bullet}$ contrary to elemental $F_2$ [37, 39-42]. Fluorinated polymers (PTFE, PVDF, CYTOP) may also act as fluorinating agents [43-47].

Nevertheless, even if this fluorination route has proven to be very efficient and reliable, the costs of both the solid fluorinating agents and the thermal process (for the decomposition and release of fluorine species) hinder its use at an industrial scale.

**Pulsed fluorination**

To minimize and even suppress the over-fluorination in the case of very reactive carbons, the progressive introduction of the elemental fluorine with successive small injections is possible (**Figure 1**). The term "pulsed fluorination" has been introduced by Ahmad et al. [4]. Without the formation of excessive defects, the expected benefits are then achieved, *i.e.,* tailoring the water content of the treated carbon thanks to more hydrophobic materials. Moreover, the thermal and chemical stabilities were enhanced without drastic structural changes and a decrease in electrical conductivity [4].

Moreover, this route allows the monitoring in real-time of the grafting thanks to the balance of the controlled injections of $F_2$ and the changes in the $F_2$ pressure inside the reactor. Grafting results in a decrease of the fluorine pressure whereas its increase evidences an over-fluorination. At the same time, the kinetics of the reaction may be followed (see **Figure 1**) which helps to maintain mild conditions.

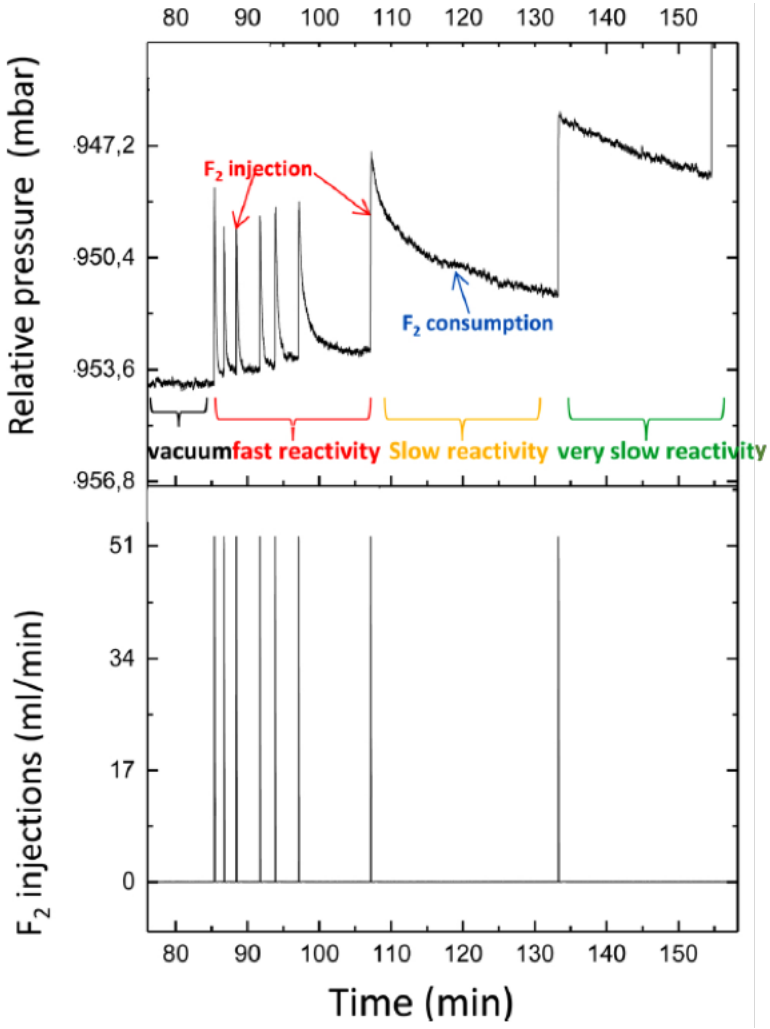


**Figure 2.** Relative pressure (mbar) and pure molecular fluorine injections (mL/min) managed at room temperature owing to pulsed fluorination method. Reproduced with permission from [4]. Copyright 2022, Elsevier.

The hydrophobic behavior of fluorinated materials can be determined by water adsorption and compared with the raw carbon and its hydrogenated counterpart [48].

**Expected benefits**

Fluorination is known for many changes in the physicochemical characteristics and, as a consequence, properties change.

First of all, the surface chemistry is modified. Polarity and surface tension are either increased or reduced, respectively [49]. The highly electronegative fluorine element is a p-type dopant that extracts electrons from carbon materials. In addition, the non-bonding doublets of the fluorine atom promote the ability of certain gases to be physisorbed.

Secondly, the reduced surface tension favors the dispersion of platinum particles onto the porous carbon. For example, Pt was well dispersed with a homogeneous particle size in [50-51]. There is a higher symbiotic impact of the fluorinated carbon matrix that favors higher catalyst dispersion and intercalation compared with classical dispersion in Vulcan XC-72R carbon black. The fluorination of carbon helps in enhancing the stability of the catalysts under acidic conditions of use [52].

Thirdly and importantly, fluorination is also known to magnify hydrophobicity. The enhancement of hydrophilicity of porous carbon materials can occur with fluorination under certain conditions, *i.e.,* applying gaseous diluted fluorine with nitrogen [53]. The enhancement of the hydrophobic character of the fluorinated sample is however the main case and was proved through higher relative adsorption pressure and its incomplete filling (56%) even at saturation pressure [54]. Superhydrophobicity can even be obtained and valuable for water management in hydrogen fuel cells [55]. A fluorine content of 1.9 at.% appears as an optimum content to put on a surface of conventional carbon black.

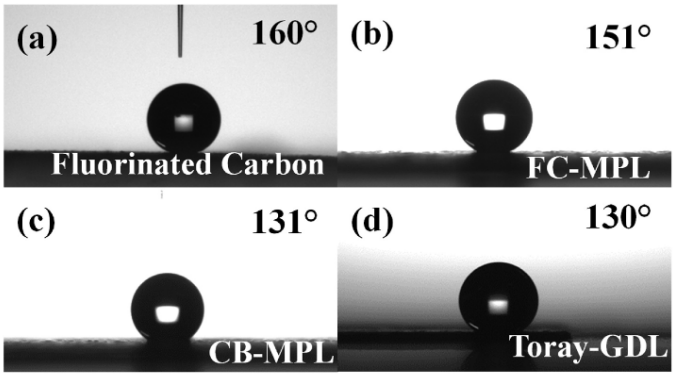


**Figure 2.** Surface water contact angle (WCA) measurements for: (a) pressed fluorinated carbon (FC); (b) Fluorinated carbon black MPL (FC-MPL); (c) Carbon black MPL (CB-MPL); and (d) TGP-H-060 Toray Paper (Toray-GDL) Reproduced with permission [55] Copyright 2022, Elsevier .

Fourthly, fluorination appears as a porosity promoter and mainly a micropore maker. As a consequence, the Specific Surface Area (SSA) can be turned by almost a 10 factor [56]. Such a change in the porosity can favor selective $H_2$ adsorption and its electrooxidation.

Benefits related to electrocatalysts will be detailed in the following parts.

### 2.2. Change in the pore size distribution

A part of the performance of the PEFCs depends both on the implementation of the catalyst layers (CLs) and the texture of the catalyst support with D interconnected pores of controllable size which are crucial and must be adapted to the characteristics of the two families of catalysts: PGM and Non-PGM electrocatalysts. Indeed, the CLs have different thicknesses and the typology (location) of the active sites differs on the catalyst supports. So, these constraints bring different challenges such as the access of reagents on the active sites and the evacuation of the water produced by the ORR. The answers come from the tuning of the texture and the hydrophobicity character to manage the mass transport (of gaseous reactant and particularly the (liquid) water produced) in the electrode to avoid flooding depending on the local wettability (electrode and catalyst surface). In addition, there is a wide consensus that increasing the specific surface area and therefore the number of possible active sites results in higher ORR activity whatever the family and prevents migration and aggregation of the catalyst.

Regarding the catalyst support itself, due to the specificity of each family, the texture requirement is different. The control of the texture is mandatory and goes through the control of the pore size distribution to allow the access of the reactants to the catalyst sites.

For the Pt-based catalysts, the present state-of-the-art consists of the deposit of 3-5 nm Pt nanoparticles (NPs) at the carbon surface from the reduction of platinum salt by chemical or physical reduction [57]. The Pt loading is classically around 40 wt%. The texture has to accommodate the deposition of Pt NPs on the carbon support and the ionomer (whose purpose is to transport the protons synthesized at the anode to the cathode via the membrane, usually Nafion®) to achieve the triple contact. Due to the size of the Pt NPs and the presence of the ionomer, micropores (< 2 nm) are useless, except for their role in liquid water sorption by capillary condensation. To obtain the higher specific surface area, the mesopores (defined between 2 and 50 nm) have to be the smallest but able to host all along Pt NPs covered by the ionomer and manage the gas and water mass transfer. According to the tortuosity of the pores, macropores (> 50 nm) are also needed and particularly when air instead of pure oxygen is used in PEFCs to evacuate water and also unreacted nitrogen.

Me-N-C catalyst materials are based on transition metals, typically Fe and/or Co, but the most actives were those based on Fe [58-59] with up to 3 wt% of atomic Fe to limit the formation of Fe NPs. The metal is coordinated to several N atoms located in particular positions on a C-C $sp^2$ network. The presence of M atoms coordinated to N atoms in pyridinic or pyrrolic positions renders the most active sites for the ORR in acid electrolytes [60]. Finally, the presence of surface

basic sites also seems to play a role in the ORR activity [57, 61]. The metal is atomically dispersed and it is well known that the active sites are located in the micropores of the catalyst [62-63]. These micropores can be obtained by the use of metal-organic-framework (MOF) as the host for Fe and N precursors [9], by the pyrolysis of the organic polymer [64] or by a thermal post-treatment with $NH_3$ (diluted or not) [63, 65]. This latter solution also brings additional N in the electrocatalyst. Nevertheless, hierarchical micro-, meso-, and macroporosity are necessary [62]. Mesopores and macropores allow to favor gas and water managements which are particularly important in these thicker CLs and enhance the utilization of the Fe-N moieties by forming channels to inaccessible sites [66]. Different methods are used by hard template method [67], by soft template method [68], by sol-gel method [64, 69], or by electrospinning of ZIF with a polymer method [11].

The modularity of the fluorination process favors a dedicated grafting in correlation with the pore size distribution. The process acting by atomic fluorine and static conditions using $F_2$ is the most suitable for diffusion up to the microporosity. Depending on the type of carbon and the fluorination conditions, all pore types can be modified [70]. To maintain a high value of the specific surface area and pore volume, porous carbonaceous must contain mesopores that are less sensitive to fluorination than micropores. However, very recently, we show that for carbon aerogel treated with $XeF_2$, even the micropore and mesopore volumes decrease meaning that mesopores can also be destroyed. Atomic fluorine released by $XeF_2$ is very reactive and acts on all the porosity types [70]. In such cases, the total porous volume increases due to higher macroporous volume and global increase of the pore size during the fluorination. This modification of the texture decreases the SSA significantly whereas the pore size distribution varies little.

The surface chemistry acts also on the relationship fluorination- pore volume evolution. For a given SSA and with similar pore size distribution, surface oxygenated groups are starting points of the fluorination as they decrease upon fluorination.

To maintain the mesoporosity, we show that the pulsed fluorination method must be favored as it allows very low fluorination atomic level F/C and reduces mesoporosity collapse to macroporosity.

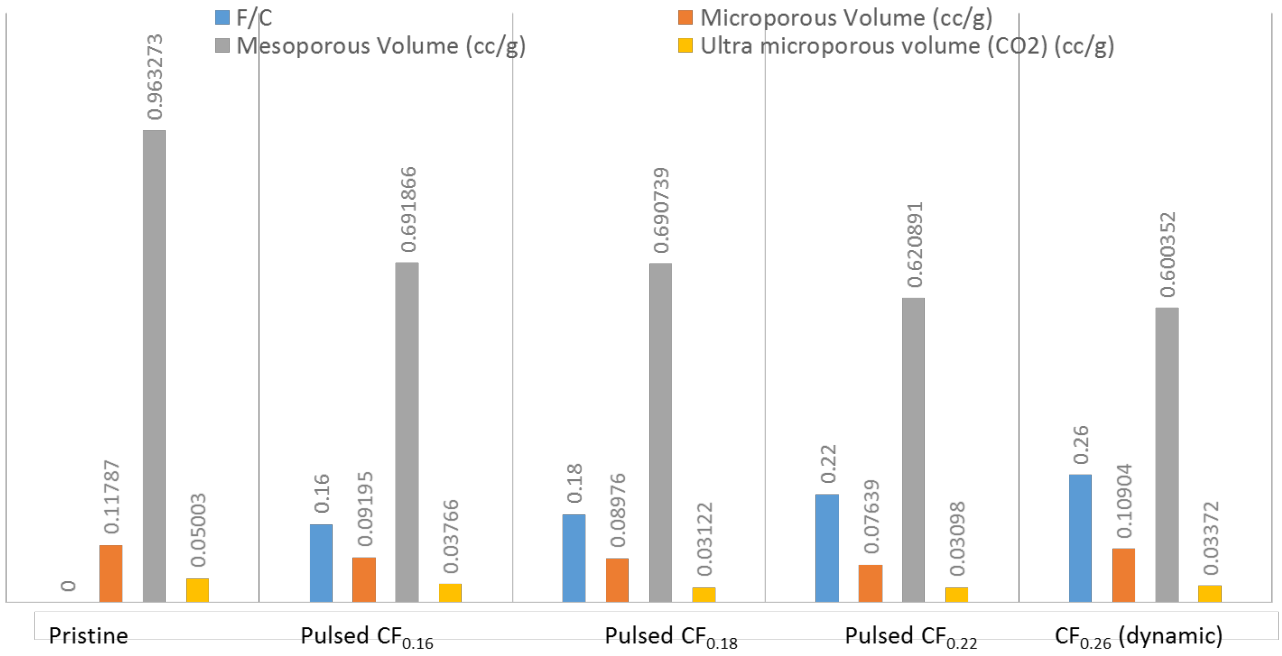


**Figure 3.** How fluorination can modulate on the microporous and mesoporous volume of a porous carbon (carbon black) as a function of F/C using pulsed and dynamic fluorinations

When pulsed fluorination is used, as the degree of fluorination increases, an incremental tendency in total pore volume, in particular, the mesoporous volume is monitored as shown in **Figure 3**. By dynamic fluorination, such progressive control does not occur and the mesoporosity is destroyed. Moreover, microporosity and ultramicroporosity (pore diameter lower than 1 nm) not useful for PEFC application are more suppressed by pulsed fluorination than direct fluorination.

For N-doped carbons, fluorination does not cause a drastic decrease in SSA (loss of 40% in the worst case). A huge decomposition of carbon in $F_2$ gas is avoided by the use of both short contact time material-gas and diluted $F_2$ with an inert gas [71].

Micropores host most of the catalytic sites in Fe-based PEM fuel cell catalysts [62] and are the more assigned by fluorination.

### 2.3. How to keep the N content in N-doped carbons

Advanced electrocatalytic activities can be achieved thanks to the doping with heteroatom that changes the surface charge/defect distributions of the carbon lattice [72-73]. The simultaneous presence of F and N (in the form of graphitic-N, pyrrolic-N, pyridinic-N, active species) increases both the C−C bond polarization and spin densities in the carbon lattice and

redistributes the charge. Co-doping is an emerging strategy to tailor the properties not only for performances of catalysts in fuel cells [74], for electrodes in supercapacitors [75], in sodium-ion batteries [76], and metal-air batteries [77] but also for information encryption and anti-counterfeiting (co-doped carbon dots [78]). One-pot solvothermal processes allow N and F co-doped carbon dots to be prepared with 4-fluorophthalic acid and glycine or as F and N sources [79] or 3, 4-difluorophenylhydrazine for both [80-81].

In addition to the favorable characteristics of a microporous conductive carbon framework, the synergistic effect between N and F dopants allows enhanced catalytic activity, methanol resistance and cycle stability to be achieved in porous carbon [82]. For this case ammonium fluoride ($NH_4F$) and dicyandiamide act as fluorine and nitrogen sources to achieve moderate co-doping (5.1 at.% and 2.5 at.% for N and F, respectively).

The N-doping with $NH_3$ may be performed with the assistance of defluorination in fluorinated Multiwalled Carbon Nanotubes [75] with nitrogen heteroatoms (about 5 at.% mainly in a pyridine-type nitrogen configuration).

Most of the co-dopings have been performed via the fluorination of N-doped carbons. According to DFT calculations and experimental data, the N-containing structure in graphene was found to be able to activate the grafting of fluorine onto surrounding carbon atoms and then guide the location of the C−F bonds [83]. The fluorination process at room temperature ($F_2/N_2$ atmosphere) has little effect on the content of N of fluorinated N-doped graphene and various porous carbons [64]. Elemental fluorine did not react directly with N in these materials whatever their type (graphitic, pyrrolic, pyridinic, hydrogenated pyridinic, or oxidized); in such a case volatile products were produced. Nevertheless, the presence of fluorine atoms changes the binding energy (BE) only for pyridinic N [64]. To the best of our knowledge, N-F bonds were never formed during fluorination.

### 2.4. Co-doping with fluorine: a general trend

If we exclude the fluorination of graphene and graphite oxides that results in the co-existence of O and F when the completion of oxygen by fluorine conversion is not achieved [31, 84-88] and in the oxidation of sub-fluorinated graphite [89], the co-doping with F and another element than nitrogen is very few reported to the best of our knowledge. $SF_6$ was used for the fluorination of S-doped amorphous carbon films for lubrication purposes [90-91] and S-doped suspended graphene. For this latter case, only sulphide component in the C-S-C configuration was detected and no other component was associated with the presence of S-F bond. As reported by Struzzi

et al. [91], the simultaneous presence of F and S allowed respectively a hydrophobic surface and the immobilization of molecules or metallic nanoparticles to be achieved.

To evidence that such co-doping can be carried out using elemental fluorine, we show here a part of the results about the fluorination of S-doped graphene (the details will be published elsewhere soon). Contrary to the case of N-doped carbons (where N-F bonds were not formed ), the formation of S-F bonds was evidenced in addition to C-F bonds by both solid-state NMR and FTIR when the fluorination conditions were mild enough, *i.e.,* 25°C or 70°C with $F_2/N_2$ (50/50 vol.%) for half or one hour (**Figure 4A**); the samples are denoted $FT_F$-duration(min), with $T_F$ the reaction temperature, *e.g.,* F25-60 min at 25°C for 60 min. In addition to the conventional vibration band at 1210 $cm^{-1}$ assigned to C-F bonds (the higher the covalence, the higher the wavenumber with a maximum at 1220 $cm^{-1}$), one doublet centered at around 932 and 922 $cm^{-1}$ was observed for fluorinated S-doped graphene. The maximum absorbance for S-F was reached for fluorination at 70°C for 1h. For C-F vibrations the higher intensity was for F140-60min; its position at 1210 $cm^{-1}$ was then related to covalent C-F bonding. On the contrary for milder fluorination conditions, a second component at a lower wavenumber was observed that evidences a dual C-F bonding; bonds with weakened covalence due to hyperconjugation between C-F and $sp^2$ C (1100 $cm^{-1}$) coexist with purely covalent C-F (1220 $cm^{-1}$). When the duration was shorter and/or the temperature lower the completion of fluorination was not achieved. On other hand, the S-F component disappeared when the fluorination temperature was increased to 140°C. This new band, never reported for fluorinated carbons, was assigned to S-F by reference [92] for $SF_4$. With the same reasoning, the additional band at +58 ppm on $^{19}F$ NMR spectra was also assigned to S-F bonds (**Figure 4B**). No corresponding band has been seen on $^{13}C$ NMR spectrum in addition to the ones of covalent C-F at 84 ppm and of non-fluorinated $sp^2$ C in the 120-135 ppm range which confirms our assignment of a new band to S-F and not C-F with S in their neighboring. The higher the fluorination temperature and the duration, the higher the F/C ratio calculated from $^{13}C$ NMR spectra, *i.e.*, 0.22, 0.51, 0.72 and 0.82 for F25-60 min, F70-30min, F70-60min and F140-min, respectively. Covalent C-F bonds, $CF_2$ and $CF_3$ groups were evidenced by lines on $^{19}F$ NMR spectra at -180, -120 and -78 ppm, respectively [42, 93-98]. It is noted that the covalence of the C-F bonds increased with the fluorination temperature. $^{19}F$ chemical shift for C-F progressively shifted from -150 to -180 ppm. Hyperconjugaison [99] is lowered when the content of non-fluorinated $sp^2$ carbons decreases. Another evidence of this phenomenon is the shift of the $^{13}C$ line for non-fluorinated $sp^2$ carbon because of the interaction with C-F bonds in their neighboring (the line is located at 122 and 134 ppm for F25-60min and F140-60min, respectively, **Figure 4C**). S2p XPS spectra

confirmed the existence of S after fluorination at 70°C (0.11 at.%) contrary to 140°C (not shown here).

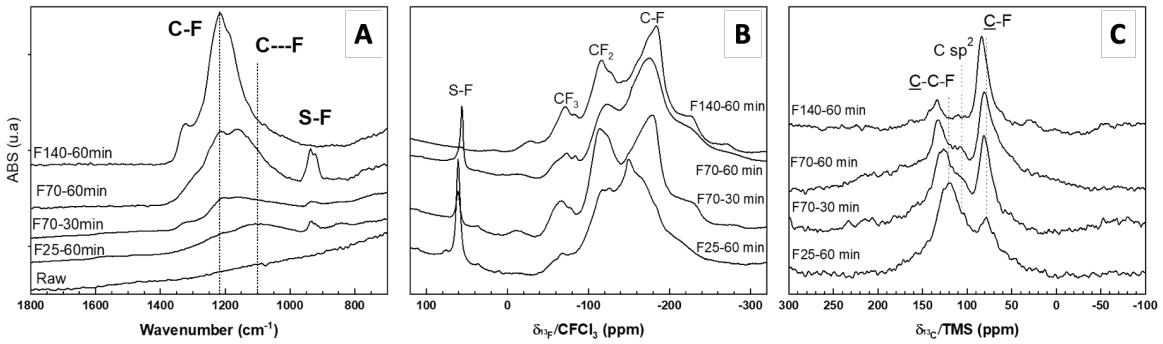


**Figure 4.** (A) FTIR spectra in ATR mode of fluorinated S-doped graphene at 25°C for 60min (F25-60 min), 70°C for 30 min (F70-30 min) and 60 min (F70-60 min), 140°C for 60 min (F140-60 min), (B) and (C) $^{19}F$ and $^{13}C$ NMR spectra of the fluorinated S-doped graphene. Recording conditions are given in supplementary information.

Co-doping with F and S is quite an unused route to tailor the physicochemical of carbons that would be further investigated. Co-doping with F and another element than N or S is also promising. Photocatalytic activity for the aqueous reduction of carbon dioxide into methanol under visible-light irradiation was excellent for P and F co-doped amorphous carbon nitride (co-doping via sol-gel-mediated thermal condensation of dicyandiamide) thanks to the narrowing the optical band gap to 1.8 eV [100]. Tri-doping of graphene materials with N, P, and F was achieved using a thermal treatment of polyaniline pre-coated graphene oxide in the presence of ammonium hexafluorophosphate; the resulting electrocatalyst was efficient for 3 electrochemical processes, *i.e.,* for ORR, oxygen evolution reaction (OER), and hydrogen evolution reaction (HER) [101]. F, N and S tri-doping may be performed during thermal defluorination in a one-step method [102], as evidenced by the change in the density of states. (DOS), both defluorination and heteroatom doping can induce the redistribution of electrons at the origin of superior electrochemical properties when those materials were used as cathodes in primary lithium batteries.

Indeed, due to the sluggish kinetics of the ORR, various types of catalysts have been developed. Carbon materials are considered either ideal catalyst supports or cathode catalysts for many electrochemical energy devices (e.g., fuel cells and metal-air batteries). In particular,

heteroatom doping is essential to boost ORR performance (e.g., activity and stability). So far, many reviews and research articles have reported the hetero-doping (e.g., N, P, S, B, Si, etc. as well as their co-/multi-doping) of carbon-based materials as catalysts for ORR reactions [103-111] including metal-free catalysts (most times limited in alkaline condition) and transition metal-based catalysts (in both acidic and alkaline conditions). However, the comprehensive review of the F-doping and their related co-doping have rarely been reported. As we have mentioned in this section, due to the intrinsic property of fluorine, the co-doping of F and other elements than nitrogen is rarely reported. However, it is possible to realize the co-doping or co-existence of F and other hetero elements in the same materials via developing different strategies and protocols. A great effort still needs to be made towards various fluorinations and their applications in electrochemical clean energy devices.

### 2.5. C-F bonding

When the carbonaceous materials exhibit a high specific surface area, at low and moderate fluorine contents, C-F bonds coexist with non-fluorinated carbons that result in hyperconjugation as defined by Sato et al. [99] and a weakening of the C-F covalency. Areas with higher fluorine content may exist in fluorinated N-doped or non-porous carbons. A dual C-F bonding, characterized by the coexistence of C-F bonds with weakened covalence (hyperconjugation) and covalent C-F, is achieved [112-113]. Irrespective of the fluorination routes, *i.e.*, using atomic or elemental fluorine, the differences in C–F bonds are due to different extents of the hyper-conjugation between non-fluorinated $sp^2$ carbons and neighboring C–F bonds in non-saturated parts. The presence of oxygenated groups may also affect the C–F bonding [31, 114].

Experimental proofs of this dual C-F bonding, *i.e.,* covalent (noted C-F) and with weakened covalence (C---F) are numerous: i) the bands at 1220 and 1110 $cm^{-1}$ in FTIR spectra are assigned respectively to C-F and C---F (**Figure 5A**) [86, 115], ii) the weakening of the C-F covalence results in a $^{19}F$ chemical shift around -150 ppm instead of -190 ppm for strong covalent C-F bonds (**Figure 5B**) [31, 84-86, 88, 93-94, 115], iii) the interaction of an $sp^2$ C and its neighbor C-F bond results in a chemical shift around 130 ppm for those non-fluorinated carbons in the $^{13}C$ NMR spectra, that is larger than the value of $\delta_{13C}$ of 120 ppm found for pure graphite. The chemical shift for C---F at 80 ppm is lower than for covalent C-F (84–90 ppm) giving additional evidence of a weakening of the C-F bonding (**Figure 5C**), iv) two peaks are observed on XPS C1s spectra at binding energy (BE) of ~ 686.8 eV for C---F bonds and ~ 688.3 eV for covalent C-F [113, 116-117], in agreement with XPS F 1s data (C-F and C---F at around 688.5 and

687 eV, respectively). The labile character of a portion of C–F bonds in fluorinated activated carbons has been shown by water adsorption [48, 112].

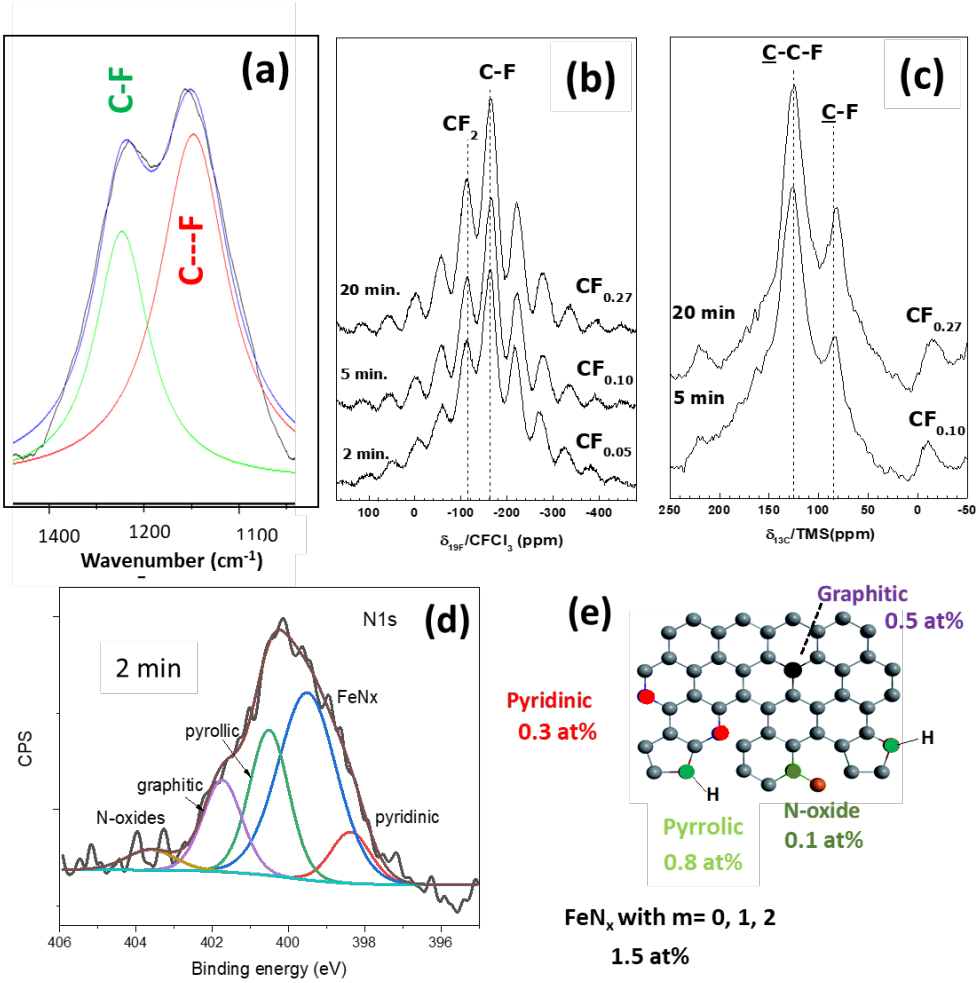


**Figure 5.** Representative example of a fluorinated porous carbon (N-doped carbon with FeNx catalyst synthesized according to the optimized conditions described in the reference [71] and fluorinated with $F_2/N_2$ (50/50 vol.%) or different durations (2, 5 and 20 min) [118] with dual C-F bonding, FTIR (A), $^{19}F$ MAS NMR (B), $^{13}C$ MAS NMR (C), and N 1s (D) spectra. A; the absolute contents for the different types of N are given in (E). Reproduced with permission [71] Copyright 2022, Elsevier

The formation of N-containing C−F bond clusters within the sheets in ultrahigh-bifunctional graphene (with N/C ratio of 0.24 and F/C ratio of 0.56) increases the number of covalent C−F bonds [83].

**2.6 Poisoning effect of fluorination on the catalysts**

Highly-defective/non-graphitized carbon aerogel (CA) supports were fluorinated by thermal decomposition of $XeF_2$ at 120°C [70]. Whatever the order of the synthesis (fluorination of the CA and then Pt deposition, or Pt deposition on the CA and then fluorination), fluorination increased the porosity of the carbon, resulting in an activation promoted by the release of reactive gases ($CF_4$, $C_2F_6$ and $PtF_6$) in the course of the reaction. Because the reaction proceeded at low temperatures, only defective carbon surface sites ($sp^3$) were bound with F species to form surface C-F groups. The presence of Pt nanoparticles on the CA (Pt/CA) prior to fluorination strongly favors the fluorination (resulting in larger F/C content) but at the expense of a severe modification of the Pt nanoparticles (which are amorphous) and of their binding to the CA support. The definition of the Pt nanoparticles over the CA or CA-F support is also impacted by the fluorination (regardless of the order of the synthesis), and fluorinated catalysts exhibit a rather larger degree of Pt nanoparticles agglomeration that the non-fluorinated Pt/CA.

With low Fe atomic content of around 1 at.% (as seen by XPS), $FeN_x$ catalytic sites do not act directly on the fluorination mechanism. Even with the lower fluorination duration (2 min), molecular fluorine reacted with iron catalysts to form fluorides as evidenced by two F1s XPS peaks, *i.e.*, Fe−F (at ~684.1 eV) and Fe−$F_2$, (~685.4 eV) [119-120]. FeNx ($FeN_4$), pyridinic, pyrrolic (or hydrogenated pyridinic), graphitic, and oxidized N were evidenced by N1s peaks at 399.5–399.8 eV, 398.3–398.8 eV, 400.6–401.3 eV, 402.1–403 eV 403.6 eV respectively (see **figure 5D and E[121]**).

A treatment with $F_2$ for only 5 min at room temperature resulted in the quasi-completion of this poisoning. C-F bonds being weaker than Fe-$F_m$ bonds (with m = 0, 1, 2), a heat-treatment with mild conditions, *i.e.,* 600°C in Ar, removed the protecting C-$F_p$ bonds (with p = 1, 2, or 3) first rather than of the poisoning Fe-$F_m$ ones. Those results evidence that the protection of the catalyst against electro-oxidation or the chemical attack by $H_2O_2$ or free radicals (that may be generated by $H_2O_2$) cannot be achieved with the present strategy.

As revealed by Fe K-edge XANES, the fluorine atoms were released from the F-$FeN_4$ and the F-$FeN_4$-F catalytic sites during the heat-treatment when the temperature was at or above 900°C. On the contrary, the heat-treatment at 600°C allowed only the N-doped carbon to be partially de-fluorinated. At 900°C or above, the Fe ion in the catalyst was reduced and recovered its initial oxidation state [118]. In other words, the $F_2$-poisoned N-doped with $FeN_x$ catalyst may be reactivated by a heat treatment in Ar.

### 2.7. Quenching of dangling bonds close to the surface

Carbon dangling bonds (DB) having a localized spin are detected by Electron paramagnetic resonance (EPR) [36, 122-124]. When the carbonaceous materials exhibit a high SSA, paramagnetic di-oxygen $O_2$ are physisorbed on the surface of carbons and may interact with the DB. Their magnetic properties are modified for the cases of graphite fluorides of $(CF)_n$ and $(C_2F)_n$ structural types [35, 85, 88] and in conducting polymers [125-126]. Paramagnetic $O_2$ species decrease the $T_1$ spin-lattice relaxation time and/or the $T_2$ spin-spin relaxation time, *i.e.*, results in a faster relaxation. The EPR linewidth ΔHpp, which is inversely proportional to $T_1$ and $T_2$, increased. This phenomenon occurs only for short DB-$O_2$ distances, typically a few nm, *i.e.,* DB located close to the surface. If this shortening of the relaxation times is huge, the broadening of the EPR signal results in its quasi-disappearance. This is the case that we have chosen to show in figure 6 for commercial porous carbons (CBe ENSACO 250). EPR spectra of raw and fluorinated carbon were recorded both in air and after out-gassing for one hour under secondary vacuum (**Figure 6**). The fluorination conditions were controlled by the number of additions in the pulsed mode (see part 2.1) to achieve increasing fluorine content, from F/C = 0.13 to F/C = 0.26. The ratio of the integrated area of the lines recorded in the air and under vacuum allows the percentage of DB close to the surface to be estimated, *i.e.,* the percentage of DB which disappeared. By this method, we were able to evidence the effect of fluorination: DB reacted with $F_2$ gas and their relative content close to the surface decreased quasi-linearly. The reversibility of the phenomena has been checked by successive vacuum/air cycles. The initial signal is recovered in each condition, air or vacuum evidencing that the quenching of DB with $O_2$ is physical and not chemical. By extrapolating the trend line in **Figure 6D**, the fluorine content must be around 0.41 to suppress all the dangling bonds located close to the surface. Nevertheless, the SSA decreases with the fluorine content (**Figure 6D**) and the extrapolated SSA at F/C equal to 0.41 is around zero $m^2/g$ which would significantly lower the electroactive surface for energy storage.

The example developed here evidences the precaution necessary for the investigation of DB using EPR to avoid underestimation of the spin density in the air for carbonaceous materials with high SSA.

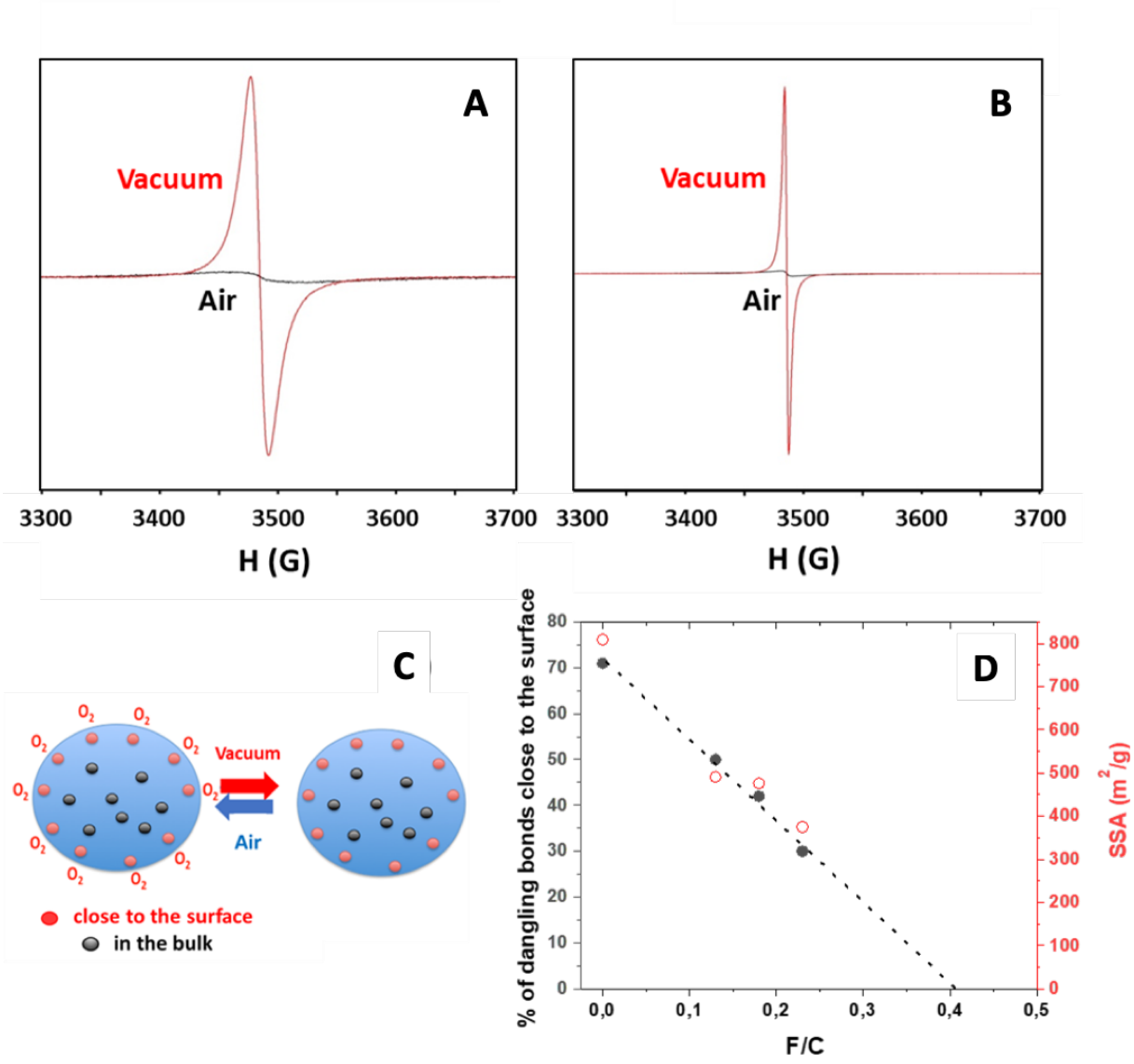


**Figure 6.** EPR spectra recorded in air and under secondary vacuum using a X band Bruker EMX spectrometer operating at 9.85 GHz for a commercial porous carbon CBe ENSACO 250 raw (A) and fluorinated (B); a scheme of the dangling bonds/$O_2$ interaction (C), the relative content of dangling bonds located close to the surface and the SSA as a function of the fluorination rate (D). Recording conditions are given in supplementary information.

Those experiments evidence another benefit of fluorination by the quenching of dangling bonds close to the surface (70% for raw and 30% for sample with F/C = 0.23). It is noted that if over-fluorination occurs, the treatment results in new dangling bonds. Once again, fluorination must be controlled to avoid such an effect.

In this section, various fluorination methods, and their effects on the bond formation and property changes of carbon-based materials have been presented and intensively discussed. To better understand the structure-property relationship of fluorinated materials and explore their

potential applications in clean energy devices, it is necessary to conduct comprehensive characterizations of the materials. Besides the elemental mapping techniques (e.g., scanning/transmission electron microscopy with energy-dispersive X-ray spectroscopy) to confirm the doping success and reveal the distribution of the doping elements, the characterization of the bond formation is essential. In this review, we have integrated the most important characterization techniques that are often used for revealing fluorination, including FTIR, Raman, XPS, NMR, EPR, and XANES. Such techniques have their different strengths (and weaknesses), and hence are complementary. As an illustration, an FTIR spectrum results from changing dipole moment whereas a Raman spectrum results from the change of polarizability of a molecule; XPS is surface sensitive and can measure the composition and the chemical and electronic states of the elements; XANES is an analytical technique used to elucidate the local electronic structure of an atom as it evolves throughout a reaction or electrochemical process, and this technique is bulk sensitive compared to XPS, etc. The combination of such techniques is recommended to comprehensively reveal the bond formation and the property of the materials. The relevance of combining experiment and theoretical simulation to clarify the underlying mechanisms of these materials must also be emphasized.

*Table 1. Primary characteristics of fluorinated (nano)carbons and methods for data collection. References provide illustrative examples.*

| | NMR* ($^{19}F$, $^{13}C$, $^{19}F \rightarrow ^{13}C$ CP) | X-ray photoelectron spectrometry (XPS) | Diffraction (X ray, electron, neutron) | Pair Distribution Function (PDF) analysis | Transmission electron microscopy (TEM) / scanning electron microscope (SEM) | Infrared spectroscopy | Raman | Near Edge X-Ray Absorption Fine Structure (NEXAFS) | X-ray Raman Scattering (XRS) | Energy-dispersive X-ray spectroscopy (EDS, EDX, EDXS or Electron energy loss spectroscopy (EELS) | Small Angle X-rays Scattering (SAXS) | Themogravimetric analysis (TGA) | Gas sorption ($N_2$, Ar, $CO_2$ $H_2O$) | Contact angles | Electrochemistry** | Atomic force microscopy (AFM) | Electron paramagnetic resonance (EPR) |
|---|---|---|---|---|---|---|---|---|---|---|---|---|---|---|---|---|---|
| **F/C (x in $CF_x$)** | [4, 34, 40-41, 113] | [127-128] | | | | | | | | [129] | | | [130-131] | | | [34, 40, 89, 102] | | |
| **C-F bonding** | [132] | [127-128] | | | | [94, 133] | | [132] | [134-135] | | [136-138] | | [130-131] | | | [34, 40, 89, 102] | | |
| **Local structural order** | [132] | | | [134-135] | | | [94] | [132] | [134-135] | | [136-138] | | | | | | | [36, 122, 124, 139-140] |
| **Long range structural order** | | | [41] | | | | [94] | | | | | | [131] | [141] | | | | |
| **Hydrophobicity** | | | | | | | | | | | | | [131] | [142] | [143-144] | | | |
| **Porosity** | | | | | | | | | | | | [145] | [131] | [141] | | | | |
| **Morphology /texture** | | | | | [146] | | | | | | | | | | [143] | | [41, 146] | [140] |
| **Thermal stability** | | | | | | | | | | | | | [41, 130] | | | | | |

(*) NMR Nuclear Magnetic resonance with Magic Angle Spinning (MAS) and Cross-polarization (CP)
(**) in a lithium battery when utilized as the cathode material

## 3. PGM electrocatalysts

It is no secret that fluorine is widely employed in electrochemical devices, specifically Li-ion batteries and fuel cells [146]. Hereafter, the emphasis is made on low-temperature fuel cell materials, in particular with platinum group metal (PGM)-based electrodes and more specifically Pt-based cathodes.

### 3.1. Fluorinated additives to tune the hydrophobicity/hydrophilicity in catalyst layers (CLs)

While the use of fluorine-based compounds is somewhat classical in gas diffusion layers (GDL) of low-temperature fuel cells/water electrolyzers [147], the number of studies where it is employed in catalyst layers is much scarcer. However, the water management in low-temperature fuel cell electrodes is very complex (water is produced in the fuel cell reaction and is necessary for ionic conduction in the membrane and ionomer of the catalyst layers (CLs), but liquid water prevents fast mass transport of the gaseous reactants inside the pores of the GDLs

and CLs), and there could be interest in tuning the hydrophillicity/phobicity of the ALs themselves.

AEMFCs are a perfect example of electrochemical systems where water management is critical. Indeed, AEMFC systems (i) operate below 100°C (where liquid water may be stable), (ii) use very hydrophilic ionomers (the water uptake in AEM is usually larger than in cation exchange membranes), and most importantly (iii) the water imbalance between water consumption at the cathode ($O_2 + 2\ H_2O + 4\ e^- \rightarrow 4\ OH^-$) and water production at the anode ($H_2 + 2\ OH^- \rightarrow 2\ H_2O$) is very large [148].

To cope with this practical difficulty, Peng et al. [149] employed PTFE additives in their catalyst layers. Increasing the PTFE content in the CLs enabled them to stably operate their AEMFCs for higher water content, with the optimized dew points continuously increasing when the PTFE content of the catalyst layer increases. This effect was explained by the better ability of the PTFE-treated anode to reject liquid water into the GDL (and not into the AEM); adding PTFE in the GDLs led to similar results.

Choi et al. did functionalize the carbon substrate of their Pt/C nanoparticles catalyst to render it more hydrophobic [150]. The functionalized carbon support was synthesized by reacting Vulcan XC-72R carbon black (which has carboxylic surface functions) with amine-terminated PNIPAM (a thermoresponsive hydrophobic polymer), which was then used to deposit Pt nanoparticles (Pt/$C_{TRP}$). The anode CL of their AEMFC was designed from this Pt/$C_{TRP}$ material, additional Vulcan XC72-R carbon (which acts as a water reservoir) and AEM ionomer. This composite enables more efficient liquid water management, the hydrophobic polymer and water reservoir favorably preventing severe anode flooding in operation. However, one does not know whether this strategy could prove stable in the long-term, owing to the limited pore volume of the added Vulcan XC72-R carbon (in other words, once saturated with liquid water, its beneficial effect on liquid water removal from the anode CL would likely be lost).

In another example, Hyun et al. proposed to tune the hydrophobicity of AEMFC catalyst layers (CLs) by using appropriately functionalized carbons to improve water management [151]. They employed hydrophilic hydroxyl-functionalized carbon additive at the cathode CL (in addition to commercial Pt/C ORR catalyst) to prevent its drying in operation, and fluoroalkyl-functionalized (fluorinated) carbon at the anode CL (in addition to commercial PtRu/C HOR catalyst) to suppress (or at least limit) flooding. Their strategy is illustrated in **Figure 7A.** Combining these functionalized carbon additives with regular commercial AEMFC catalysts so to enhance the hydrophobicity of the anode CL and the hydrophilicity of the cathode CL led to an increase of the maximum current density by 1.7 times versus the MEA without carbon-

additive (**Figure 7B**). Importantly, the strategy seems robust in the long run, as the stable constant current operation was possible for 1000 h (**Figure 7C),** which illustrates that water imbalance between the cathode and anode could be efficiently mitigated by tuning the electrodes' hydrophilic/hydrophobic behaviors.

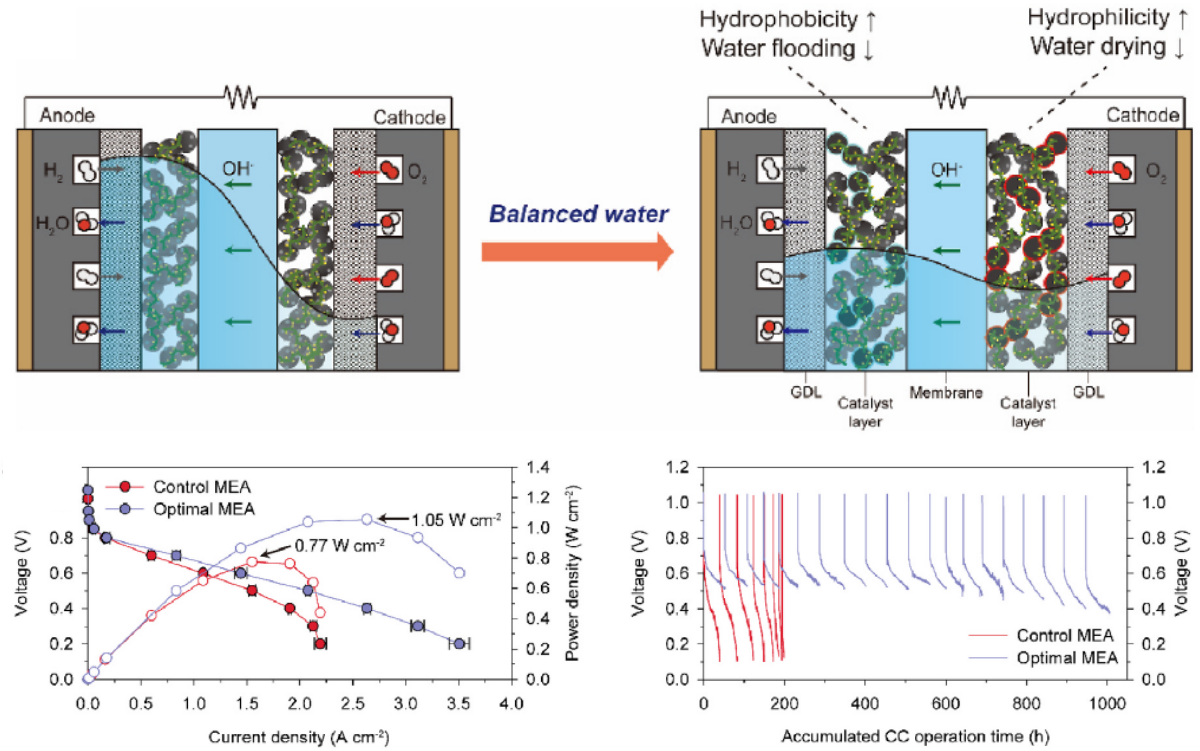


**Figure 7.** (A) Illustration of the strategy of Hyun et al. to tailor the carbon hydrophilicity/hydrophobicity within the active layers of AEMFC so to better manage liquid water. (B) Corresponding polarization curves and power density plots obtained for control AEMFC MEA (without treated carbon additives in the CLs) and optimized AEMFC MEA, and (C) long-term operation voltage at j = 0.6 A $cm^{-2}$ (constant versus time). The single cells were operated at 60°C and 100% RH without back-pressure. Reproduced with permission from [151] Copyright 2022, Elsevier.

Although water management is not as critical in PEMFCs as in AEMFCs, one must recognize that cathode flooding is a serious impediment in PEMFCs as well. The usual strategies to cope with liquid water management in PEMFCs are usually based on tightly controlling the operating conditions of the system (RH%, fluxes and temperature). Another strategy, not specific to PEMFC, is to include the hydrophobic agent in PEMFC cathodes. This has for example been performed by Ouattara-Brigaudet et al., where they tuned the ionomer-to-carbon ratio and added significant PTFE in the cathode CL to improve the PEMFC performance, with electrodes based on carbon aerogel catalysts substrates [152].

A similar strategy was later followed to prepare composite PVDF and Pt/C by electrospinning. The so-obtained composite-structure electrodes exhibited enhanced hydrophobicity, which rendered the expulsion of water more efficient, hence decreasing the carbon corrosion rate; as a result, cathode collapse was retarded, even when some carbon loss was experienced in the cathode and its porosity was increasing. Nevertheless, the added PVDF was found to dilute the ionomer and lower the proton conductivity of the binder. All in all, the drawbacks of PVDF addition in an ionomer/PVDF cathode binder (increase in protonic resistance, PVDF being uncharged), which reduces the MEA power output, was positively counterbalanced by the composite structure (that persists throughout the carbon corrosion AST).

Anodes of direct alcohol fuel cells incorporating PVDF as a binder and hydrophobic agent have also been prepared by electrospinning of PVDF and graphitic carbon nitride-supported Pd nanoparticles [153]. Another example is the electrospun Pt-based and PVDF-containing PEMFC electrodes (PVDF/Pt/C/S-$SiO_2$, PVDF/Pt/C/Nafion), with tailored hydrophilicity for dry operation [154].

### 3.2. Fluorinated carbons to modify the catalytic properties

Chemically modifying carbon structures to enhance their ORR activity is very popular in the field of low-temperature fuel cells. While the most-employed methodology is to combine nitrogen and metal doping, as pioneered by the group of Dodelet [8], other strategies have been put forth, and among others, fluorination as described previously.

For example, Liu et al. [155] demonstrated that fluorine and chlorine co-doped carbons could approach the ORR activity of commercial Pt/C catalysts for the ORR in alkaline environments. The stability of the F, Cl-doped carbon catalyst also proved interesting, as its ability to tolerate the presence of methanol in the electrolyte. The same conclusions were reached by Wang et al. with fluorine-doped mesoporous carbons [156]. Many other papers dealing with non-Pt group metal-base (non-PGM-based) catalysts have since then been published, which will be dealt with in **Section 4** of the present contribution.

Fluorine doping is also a strategy of choice to improve the conductivity of some metal-oxide supports (*e.g.,* F-doped tin oxides [157-158], but such methodologies will not be further developed hereafter, owing to the uncertainty of the practical interest of metal oxide supports in PEMFC, as they can have a deleterious effect on the membrane [159] and their durability in operation is not granted [160].

### 3.3. Fluorinated carbon supports to enhance the durability of Pt-based catalysts

Carbon corrosion is thermodynamically favorable in water-containing electrolytes as soon as the electrode potential exceeds ca. 0.2 V vs RHE; this means that carbon corrosion is theoretically unavoidable in PEMFC (and AEMFC) cathodes. Carbon support corrosion is amongst the most important threat to the PEMFC durability in operation [161-162]. Carbon corrosion leads to detachment/migration of the Pt catalysts particles (hence to loss of electrochemical surface area, ECSA, and therefore loss of activity), but also to hydrophilization of the catalyst layer and loss of its porous structure, which both compromise the mass-transport properties of the cathode.

The mechanisms of carbon degradation are now well understood: for example, in acidic electrolytes, at low potential ($E$ < 1 V vs RHE), carbon corrosion is likely occurring for defective carbon structures, and graphitic carbons are more robust (**Figure 8**). The presence of Pt catalyst nanoparticles is however prone to modify the fate of the carbon substrate, Pt-induced carbon corrosion being likely in the potential region where the Pt/Pt-OH transition proceeds, *i.e.,* in the interval 0.6 < $E$ < 1 V vs RHE. The same Pt-catalyzed carbon corrosion also proceeds in alkaline environments [163-165], although in that case, it specifically leads to Pt nanoparticles detachment from the carbon support and carbon hydrophilization, leading to dissolution (flacking off) of full graphene layers [166]. Above ca. 1 V vs RHE, Pt is fully oxidized (passivated), and so high potential (1 < $E$ < 1.5 V vs RHE) carbon corrosion becomes essentially not catalyzed by Pt ("intrinsic"), being faster for amorphous than for graphitic carbon surfaces [167-168]. In essence, carbon corrosion (should it be catalyzed by Pt at low potential, or not), initiates by the oxidation of carbon oxygenated surface functions ($CO_{ad}$ or $COH_{ad}$), which further react with water ($H_2O$) or with Pt-$OH_{ad}$ species into $CO_2$.

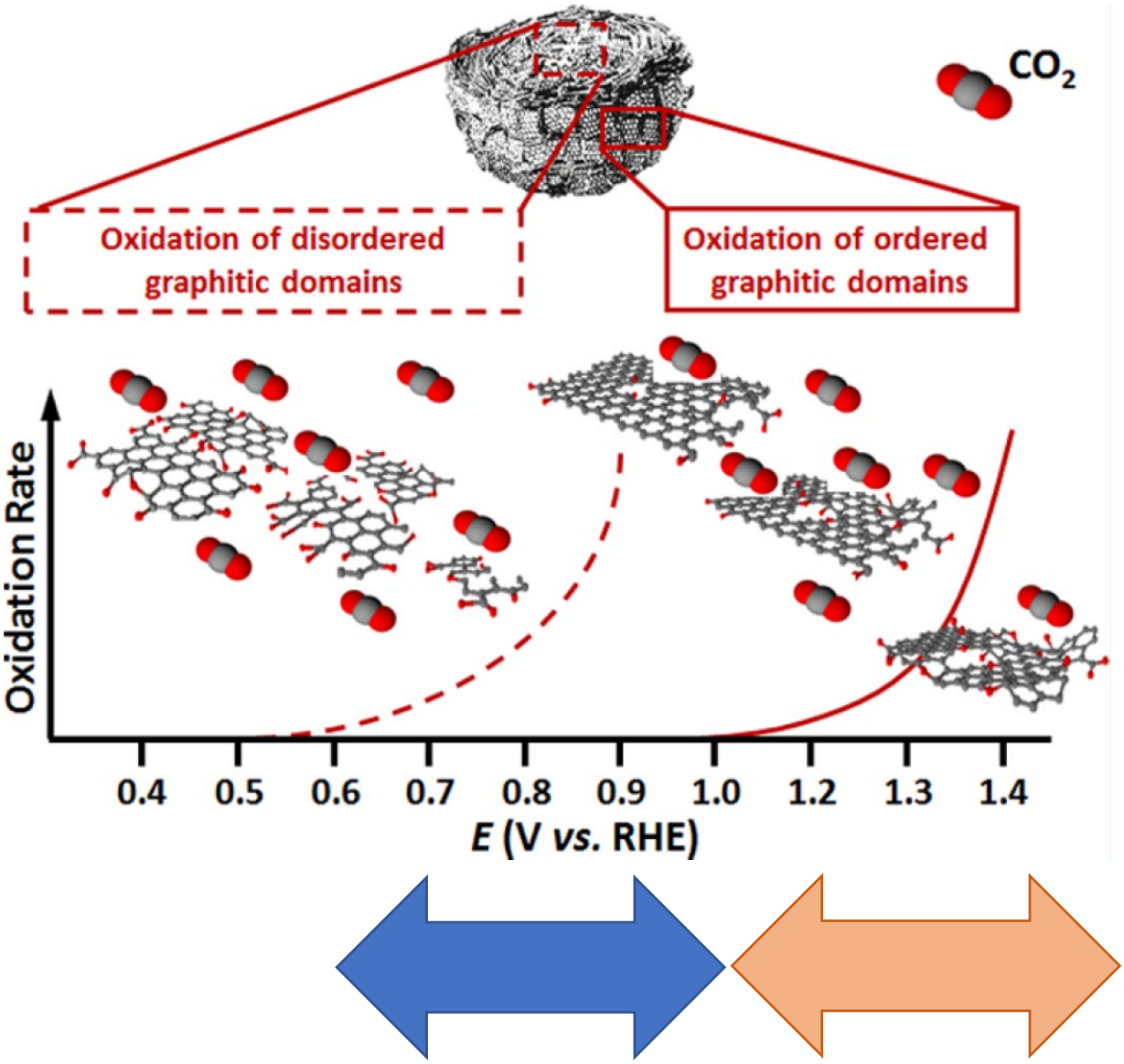


**Figure 8.** Illustration of the effect of the electrode potential on the corrosion of carbon supports; disordered carbon surfaces are more prone to be irreversibly corroded into $CO_2$ at low potential (E < 1 V vs RHE), while more ordered carbon surfaces (graphitic) require larger potential to be oxygen-functionalized and then corroded into $CO_2$ (E > 1 V vs RHE). In the meantime, Pt can assist carbon corrosion via a Pt/Pt-OH surface redox shuttle when not fully surface oxidized, which is likely between 0.6 < E < 1 V vs RHE. Freely-adapted from [162] , Copyright 2022, with permission from the American Chemical Society.

This mechanism is now well-admitted, and its knowledge has led the scientific community to look for manners to limit/retard the formation of oxygenated surface functions on carbon surfaces, so limit/retard irreversible carbon corrosion into $CO_2$ and associated loss of performance of PEMFC (and AEMFC).

In that context, Forouzandeh et al. modified the surface of a mesoporous carbon powder (CIC, highly hydrophilic), and a microporous Vulcan carbon (VC, mildly hydrophobic), to render them more robust against oxidation. The functionalization was performed by diazonium reduction, leading to 2,3,4,5,6-pentafluorophenyl (-$PhF_5$) surface groups at the carbon substrates. These carbons were then subjected to severe potential cycling [1.4 V vs RHE (50 s) - 0.8 V vs RHE (10 s)] at room temperature in 0.5 M $H_2SO_4$, so to test their robustness against corrosion. The surface functionalization improved the corrosion resistance by ca. 50–80%, which was explained by combined surface passivation (loss of carbon active sites that can be corroded) and increased surface hydrophobicity, water being required to initiate carbon corrosion (**Figure 9**)[169]. The work was pursued by evaluating as well hydrophilic functionalization of the carbon surface ($PhSO_3H$ groups), which also lead to some protection of the underlying carbon [170], these materials being advantageously employed as microporous layer (MPL) materials of GDL [171]. However, these studies did unfortunately not explore such protected carbon-baring Pt nanoparticles for PEMFC applications.

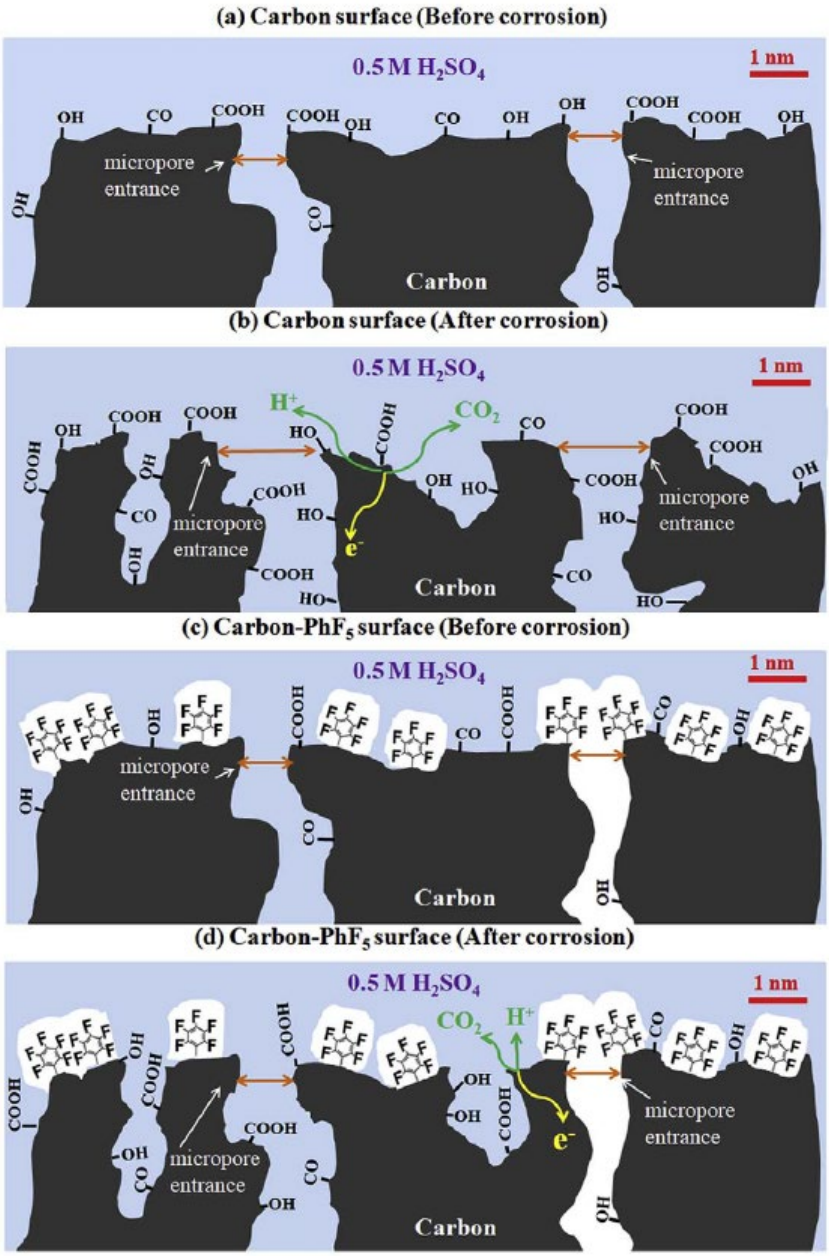


**Figure 9.** Illustration of the surface modifications occurring for bare and fluorine-functionalized ($PhF_5$ surface) VC and CIC carbons, (a,c) before and (b,d) after accelerated corrosion experiments. Formation of new pores or deepening of existing pores are likely on regions of the carbon that are not protected by the PhF5 surface groups. Reproduced from [169] Copyright 2022, with permission from Elsevier.

A step further was made by Gouse Peera et al.[172], who synthesized N and F co-doped graphene nanofibers (GNF) to immobilize Pt nanoparticles, and used the obtained materials in PEMFC cathodes. They noted the beneficial effect of the double surface functionalization of the GNF on the interactions of the Pt nanoparticles with their N,F-doped GNF substrate, leading to their more homogeneous distribution at the GNF surface, which led to high ECSA of the obtained

catalyst and related higher ORR activity. This stabilization of the Pt nanoparticles at the N,F-doped GNF substrate also proved beneficial upon accelerated stress tests, the multifunctional catalyst being more stable than a Pt/C benchmark in both low potential cycling ($0 < E < 1.05$ V vs RHE) and high potential hold ($E$ = 1.4 V vs RHE) experiments. It was posited that the presence of F groups at the carbon surface enhances the durability of the GNF substrate: F being more stable at the edges than in the interior region stabilizes the carbon edges, hence making the carbon grains more resistant to corrosion.

In a similar approach, Akula et al. evaluated N,F co-doped graphitic carbon fibers for the preparation and use of Pt nanoparticles in the ORR at PEMFC cathodes [173]. They noted the improved ORR performance and durability upon accelerated stress test of the Pt/N,F-doped GNF materials versus their N,F-free counterpart, which they ascribed to enhanced (stronger) interaction of the Pt nanoparticles with the N,F-doped GNF substrate. This was further demonstrated in PEMFC, but unfortunately in poorly-realistic conditions for practical applications (pure $O_2$ feed, high stoichiometry, 100%RH).

Park et al., by grafting F-containing diazonium moieties to Pt/catalysts, noted an improvement in the catalyst durability, which they ascribed to the modified wettability of the catalyst [174].

Some of the authors of the paper have adopted another (more direct) approach to selectively fluorinate a highly-defective/non-graphitized carbon aerogel supports (see section 2.6); the bare CA and fluorinated CA were used as the substrate for Pt nanoparticles deposition using the water-in-oil method, and fluorination was also attempted on pre-synthesized CA-supported Pt nanoparticles [70]. Despite the unsatisfactory dispersion of the Pt nanoparticles on the fluorinated carbon supports, the initial ORR specific activity of the F-Pt/CA (where fluorination was performed after Pt deposition of the CA support) did match those of the non-fluorinated Pt/CA sample and exceeded that of commercial Pt/Vulcan XC72 (the latter presenting smaller Pt nanoparticles, that are less ORR specific active). The F-Pt/CA sample proved somewhat durable in so-called base-load (0.6 – 1.05 V *vs* RHE) accelerated stress tests (AST) performed in 3-electrode cell (liquid acidic electrolyte): it maintains better its ECSA than the non-fluorinated Pt/CA and the commercial Pt/Vulcan XC72 samples; unfortunately, at that stage, this interesting behavior had not been explained.

In a refinement of the previous study, the methodology of fluorination was adapted (direct partial reaction of $F_2$ at the desired carbon support in the gas phase) to render it compatible with the up-scaling of the synthesis; it was performed with a variety of commercially-available carbon supports, Then, Pt nanoparticles were immobilized at the surface of the bare and of the

fluorinated carbon supports using a colloidal polyol synthesis, where the Pt colloid size was kept constant for all the materials. The obtained catalysts had similar Pt crystallite sizes for all the samples, which shows that the new methodology of synthesis of the Pt nanoparticles was better controlled than in reference [70]. The extent of Pt nanoparticles agglomeration was found to depend mainly on the available carbon surface area, not so much on the nature of the carbon-fluorine surface chemistry (except at large F/C ratios, for which the bulk carbon structure started to be modified). In terms of electrochemical properties, the ECSA of the non-fluorinated carbons scales with the BET surface area of the support (**Figure 10C**). This trend is modified after the fluorination of the carbons because the partial occupation of carbon dangling groups by F atoms reduces the local stabilization of the Pt nanoparticles in these regions and decreases the ECSA of the fluorinated amorphous carbons (EN and CA); on the contrary, the partial amorphization induced by fluorination of the graphitic YS carbon enhances the Pt nanoparticles-substrate interaction: higher fluorination rate led to larger ECSA and lower extent of Pt nanoparticles agglomeration for the fluorinated graphitic carbon support. This shows that fluorination increased the number of defective carbon sites (by destructing initially-present graphitic C-C bounds and creating C-F bounds). For the bare carbon supports, the ORR specific activity is inversely proportional to the ECSA (hence to the carbon supports' BET surface area), but directly with the extent of Pt nanoparticles agglomeration. All the fluorinated carbon samples are more active than their bare carbon equivalents, which was ascribed to the non-negligible intrinsic activity of fluorinated carbon for the ORR (see section 4).

Then, the materials were evaluated in an accelerated stress test in a 3-electrode cell (liquid electrolyte, **Figure 10**).

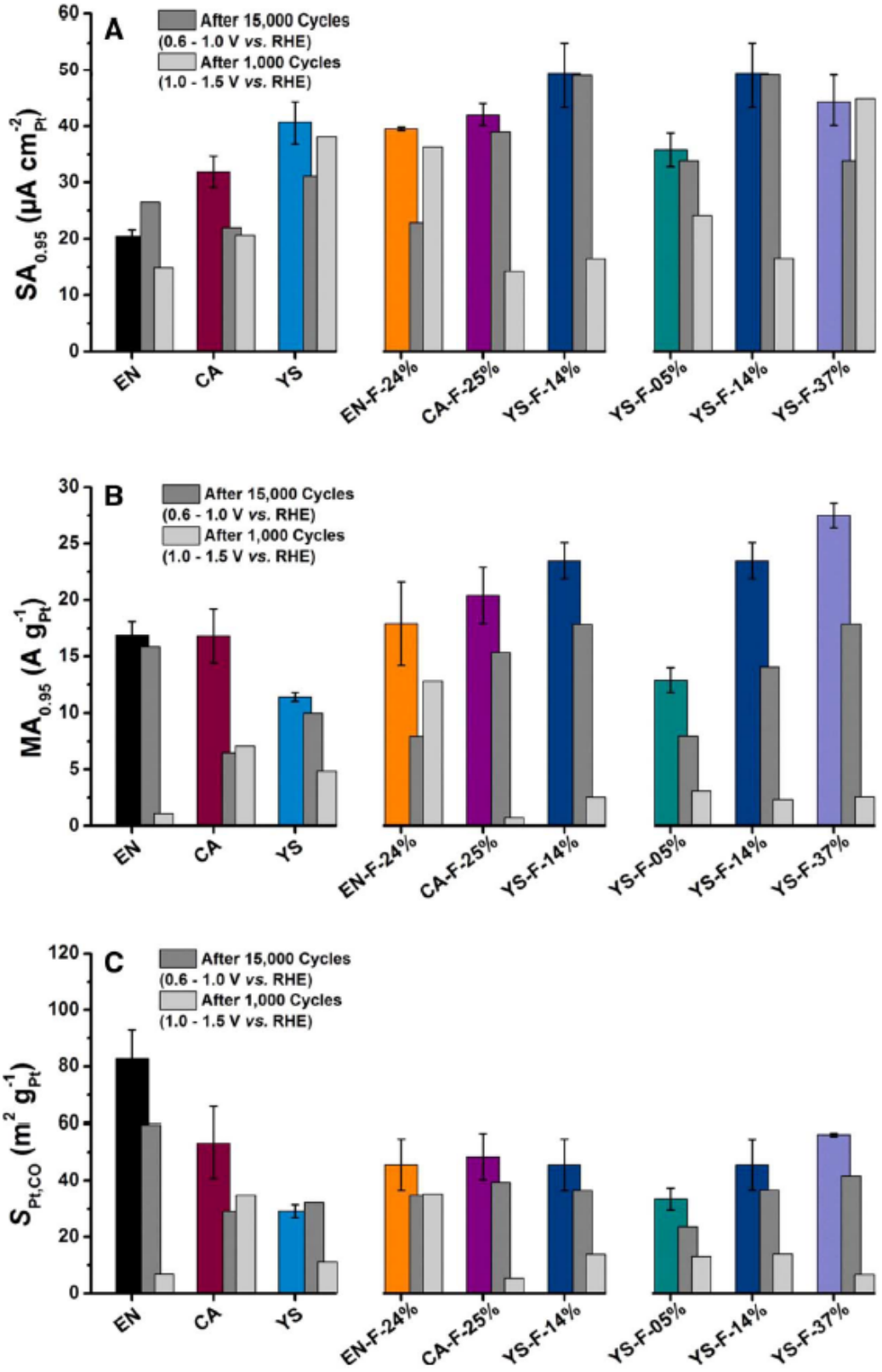


**Figure 10.** Electrochemical properties of various fluorinated or not Pt/C samples measured in 3 electrode cell (0.1 M $HClO_4$ at T = 25°C) before (Fresh) and after 15,000 cycles of base-load AST (0.6 < E < 1.0 V vs. RHE) or after 1000 cycles of start-up/shut-down AST (1.0 < E < 1.5 V vs. RHE) performed in 0.1 M $HClO_4$ at T = 80°C. (A) Specific activity (SA0.95) and (B) mass activity (MA0.95) of ORR measured at E = 0.95 V vs. RHE after mass-transport and

ohmic-drop correction. (C) Electrochemical surface areas of platinum ($S_{Pt,CO}$) measured from the coulometry of the CO-stripping peak. Reproduced from [51] with permission from the Electrochemical Society.

The base-load AST has a non-negligible (but expected) effect on the catalyst materials: it triggers Ostwald ripening and related ECSA (and ORR activity) losses (**Figure 10**), without significant carbon support corrosion. Neither graphitic carbon (YS) nor fluorinated ones show any real trend in "protection" against such degradations in this test, because (i) it mainly harms the Pt nanoparticles and not their substrate and (ii) if any carbon corrosion occurs, it is mainly catalyzed by Pt and not intrinsic to the carbon support.

Of course, the picture changes for the start-stop AST, which is much more aggressive to the carbon support (**Figure 10**). Although C-F surface groups are theoretically stronger than C-O ones, partially-fluorinated CA does not efficiently protect the amorphous carbon support, with non-protected (non-fluorinated) regions of the CA acting as "sacrificial regions" in the carbon corrosion process. The partially-graphitic EN sample, after partial fluorination (EN-F), demonstrated a very decent stability to the start-stop AST: its C-F bonds were found more robust than the initial C-O bonds of amorphous regions of the non-fluorinated EN carbon, which, together with the non-negligible presence of graphitic regions in EN, rendered the EN-F more robust in start-stop operation. Finally, the graphitic carbon (YS) exhibited no beneficial impact of fluorination, because rather stable C-C bounds are broken upon fluorination to form C-F bounds, that are not more robust than graphitic C-C bounds versus carbon corrosion (at least in aqueous acidic electrolytes, *i.e.*, in presence of excess water). So, in conclusion, the beneficial (or not) effect of fluorination depends on the nature of the carbon support employed. Fluorination is more beneficial for partially structurally disordered/ordered carbons than for structurally-ordered or structurally-disordered carbons. Indeed, "free" dangling groups of disordered regions of the partially-defective carbon supports (which, when unprotected, are subjected to preferential oxidation in PEMFC cathodes), react with the fluorine precursors to form more robust C-F bounds that are less prone to oxidation, while on the contrary, fluorination of structurally-ordered graphitic regions generates C-C bond cleavage, hence structural disorder and depreciated resistance to electrochemical corrosion.

Based on these results, some of the materials were upscaled: Pt nanoparticles deposited on the partially-fluorinated YS catalyst (YS-F) were tested in unit PEMFC, in comparison to Pt nanoparticles deposited on the non-fluorinated YS and a commercial Pt catalyst based on

graphitic carbon black (Tanaka TKK TEC10EA40E) [175]. It was notably tested whether the robustness of fluorinated carbons versus carbon corrosion could change in a polymer electrolyte environment, *i.e.*, In absence of excess liquid water.

The home-made membrane electrode assemblies (MEAs) perform close to the commercial reference, both in terms of ECSA (**Figure 11A**) and of activity (**Figure 11B**), the fluorinated cathode (YS-F 14%) showing slight depreciated initial performances compared to the non-fluorinated cathodes (likely because the MEA formulation could not be optimized in this study). Then, the MEAs were submitted to the base-load and start-stop ASTs in unit PEMFC.

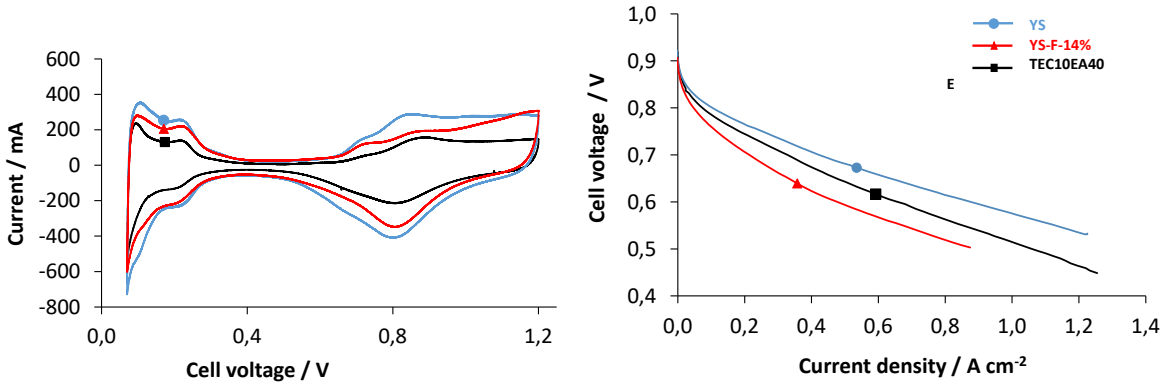


**Figure 11.** (A) ECSA characterizations of the MEA using the home-made Pt/YS (non-fluorinated), Pt/YS-F (fluorinated) graphitic carbon and commercial Tanaka TKK TEC10EA40E at the cathode, and (B) corresponding polarization plots in unit PEMFC. Reproduced from [175] with permission from Elsevier. The readers are directed to the original paper for complete experimental details.

As in a liquid electrolyte environment, the effect of the YS carbon fluorination is unclear for the "load-cycling" protocol ($0.6 < E < 1$ V): benchmark TEC10EA40E-based MEAs are more durable than fluorinated (or not) YS-based MEAs, the main degradation phenomenon in this AST being Ostwald ripening of the Pt nanoparticles. Overall the base-load AST resulted in a small loss of performance for the three cathodes (**Figures 12A, C, E**).

On the contrary, the fluorinated YS-F electrocatalyst is more durable than the bare YS in the start-stop AST ($1 < E < 1.5$ V, **Figure 12B, D**). The ECSA and activity losses are minored for the fluorinated YS-F cathode compared to the non-fluorinated YS cathode, signing that fluorinated carbons are more corrosion-resistant in polymer electrolyte environment than in liquid electrolyte. Raman spectroscopy confirmed the beneficial effect of the fluorination towards carbon corrosion in polymer electrolyte environment in the startup-shutdown AST, while TEM micrographs showed that the YS carbon fluorination led to more resistant Pt

nanoparticles versus sintering and growth phenomena during this AST. However, the commercial catalyst material TEC10EA40E (Pt on graphitized carbon black) remained the more robust in both ASTs and specifically the start-stop one (**Figure 12F**). The latter finding was associated with (i) a better optimization of the MEAs and (ii) a different manner to synthesize the Pt nanoparticles than on the home-made carbon substrates, but it nevertheless raises questions towards the real benefit of fluorination of initially graphitic carbons to enhance its carbon corrosion resistance. It would thus be important to confirm in PEMFC tests that partially-graphitic carbon can indeed be efficiently protected by partial fluorination, as put forth in [51] and recalled above.

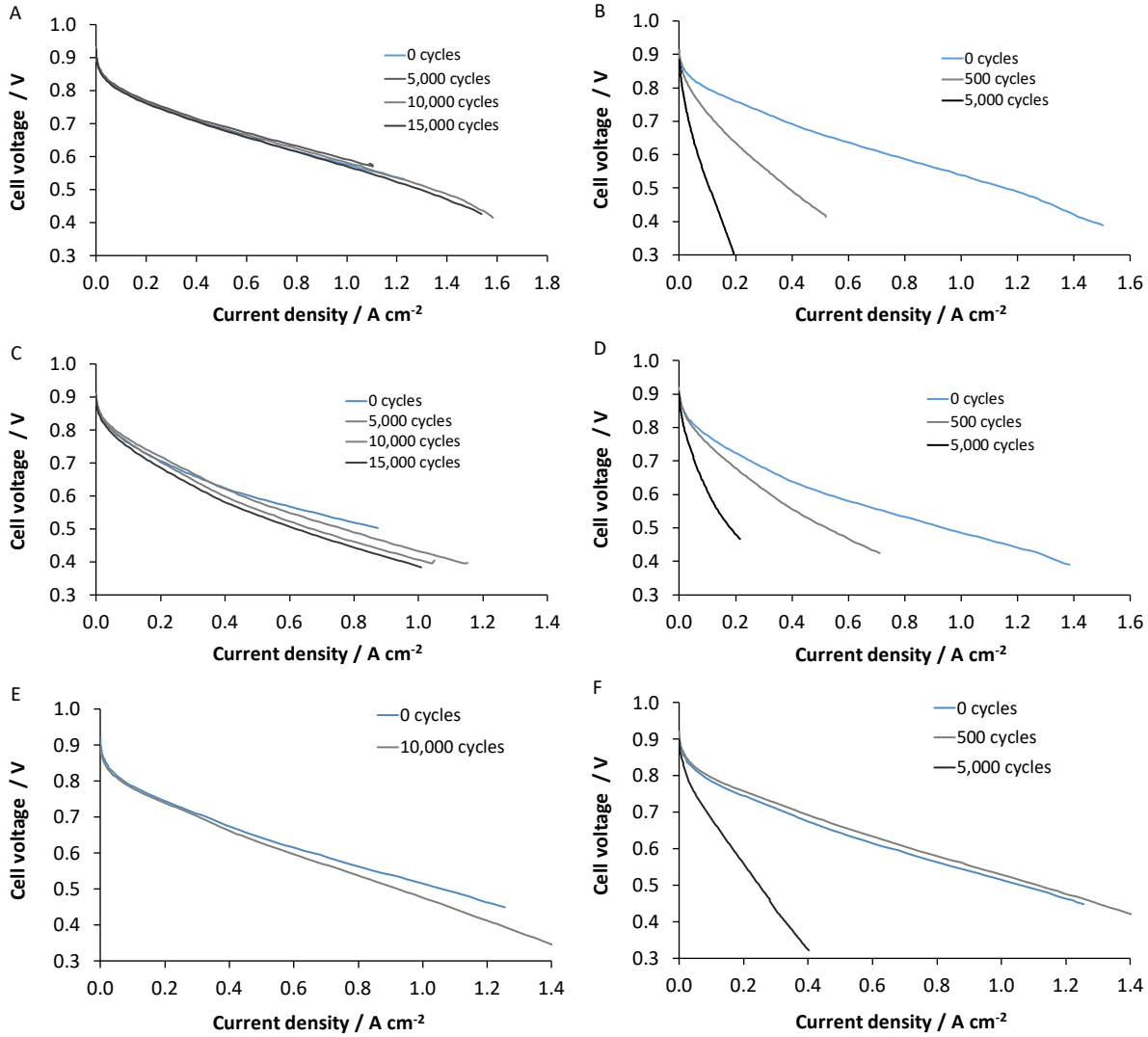


**Figure 12.** Polarization plots of unit PEMFC based on a YS cathode (A, B), YS-F-14% cathode (C, D) or TEC10E40E1 cathode (E, F) during the base-load AST1 (A, C, E) or start-stop AST2 (B, D, F) protocols. The operating conditions employed for the ECSA CVs and AST are summarized in Table 2 in the original article. Reproduced from [175]. Copyright 2022 with permission from Elsevier.

Since this study, others claimed that the impact of F-modified carbon structures was beneficial, which was explained in the frame of lower adsorption energy of $H_2O$ on F-modified carbon versus their bare counterparts, which improves the carbon support corrosion resistance [176]. From the authors' point of view, this blur in the potential protective effect of fluorination for PGM-supported PEMFC catalysts means that more work is desired to find the proper strategy to protect carbon supports for long-term PEMFC operation.

The next section 4 will show whether fluorination is more adapted to non-PGM catalysts.

## 4. PGM-free electrocatalysts

In recent years, great efforts have been made for seeking alternative and inexpensive catalysts to substitute Pt-based catalysts, such as metal-free catalysts [72, 177-178] and platinum-group-metal free (PGM-free) catalysts [8-9, 12-13, 179-181].

### 4.1 Fluorinated metal-free catalysts on fuel cell activity and stability

Metal-free catalysts, especially carbon-based ones (*e.g.,* high surface area carbon blacks, carbon nanotubes, graphene, etc.) with various heteroatoms (N, P, S, B, etc.) have been demonstrated to exhibit excellent ORR catalytic performance. However, it is worth noting that they are, most time, active in alkaline electrolytes, not in acidic conditions. To further improve their activity and stability, some researchers have employed the fluorination technique [182-189]. Notably, people have discovered the co-doping of carbon materials to form dual–doping even trinary–doping electrocatalysts. For example, Jiang and his co-workers [189] successfully fabricated a dual (NF)-doped graphene with mesoporous structure (NF–MG), through high-temperature treating the graphene oxide and polyaniline (GO/PANI) as well as $NH_4F$. **Figure 13A** demonstrates a uniform distribution of C, N, O, and F loading in the mesoporous graphene framework. Due to the synergy of F and N co-doping into the hierarchical graphene, the oxygen reduction property of NF–$MG_3$ (i.e., the optimal catalyst) is comparable to the commercial Pt/C catalyst in the alkaline solution (**Figure 13B).** In addition, this catalyst shows a super-low $HO_2^-$ yield (**Figure 13C),** and a high electron transfer between 3.81 and 3.94 (**Figure 13D)**. The very low $HO_2^-$ yield is supposed to be able to greatly hinder the degradation of the membrane and the electrocatalysts and thus cell performance. In addition, this NF–$MG_3$ nanosheet material exhibits not only superior tolerance to methanol crossover effects but also excellent long-term stabilities in alkaline media than the commercial Pt/C catalyst (**Figure 13E-H)**. Thus, this type

of catalyst holds great potential for use in direct-methanol alkaline fuel cells, especially suitable for the system without an ion exchange membrane.

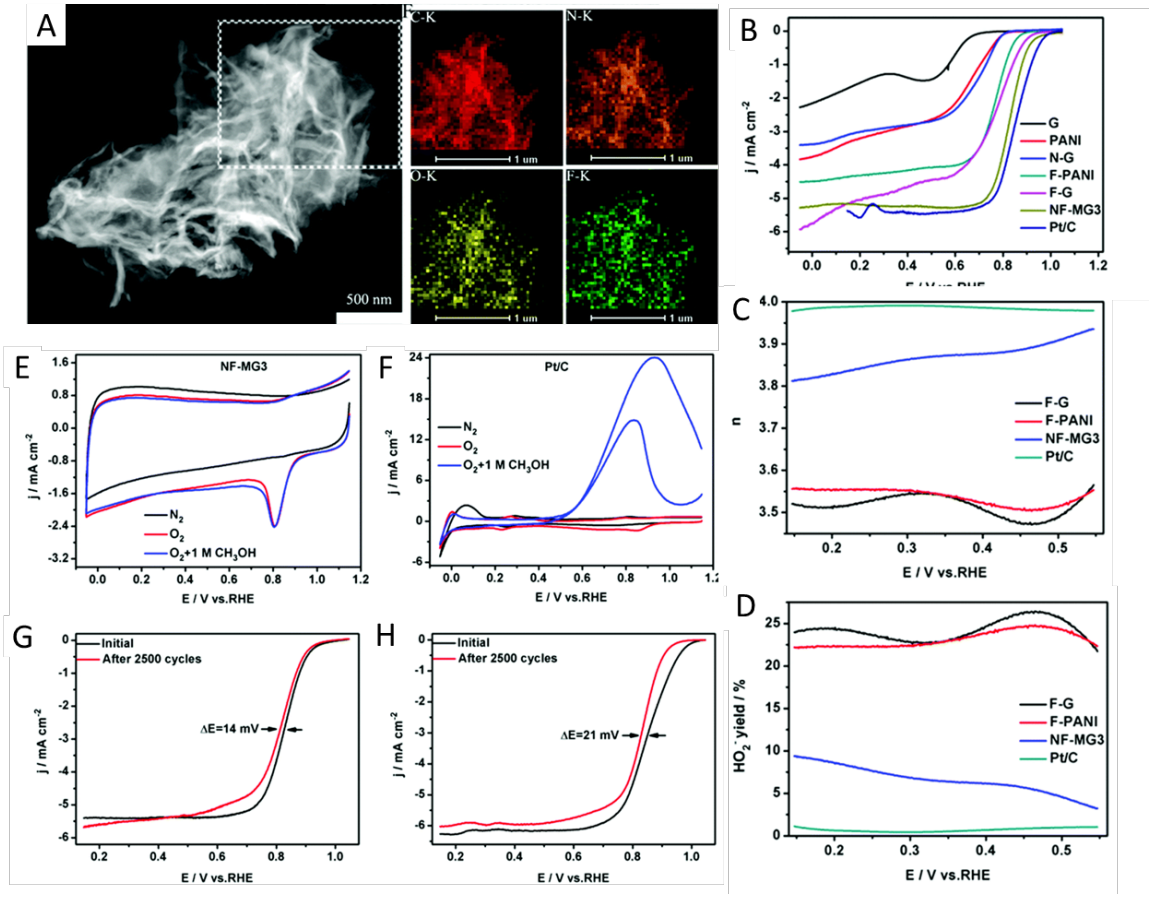


**Figure 13.** (A) annular dark-field (ADF)-STEM image of NF–MG3, and elemental mappings for carbon, nitrogen, oxygen, and fluorine. (B) ORR polarization curves in an $O_2$-saturated 0.1 M KOH solution (10 mV $s^{-1}$, 1600 rpm). (C) electron transfer number n and (D) $HO_2^-$ yield. (E-H) The methanol tolerance of NF–MG3 (E) and Pt/C (F), in 0.1 M KOH solution saturated with oxygen, as well as the excellent stability curves of NF–MG3 (G) and Pt/C (H). Reproduced from [189] with permission from the Royal Society of Chemistry.

### 4.2 Fluorinated non-PGM catalysts on fuel cell activity and stability (advances and drawbacks)

Non-PGM catalysts have been stimulated more extensively, especially by the recent push for proton exchange membrane (PEM) fuel cell commercialization, the high cost of Pt-based materials, and the lower performance of the metal-free catalyst in acidic media. From the literature review, several important types of non-PGM catalysts for ORR have been reported, such as pyrolyzed [190] and non-pyrolyzed [10] transition-metal nitrogen-containing complexes,

conductive polymer-based materials [191], transition-metal chalcogenides [192], metal oxides/nitrides/carbides/carbonitrides/oxynitrides[193], as well as enzymatic compound materials [194]. Among these materials, pyrolyzed M/N/C catalysts (M is a transition metal) are considered the most promising ORR catalysts. One breakthrough has been made by the Dodelet group at INRS with catalyst activity and performance (0.91 W/cm$^2$) approaching that of Pt [9]. This type of catalyst (Fe/N/ZIF-8) was prepared by doping a commercially available microporous metal-organic framework (MOF) known as ZIF-8 with a coordination complex of iron(II) acetate and phenanthroline, followed by Ar and $NH_3$ two-step pyrolysis, respectively. Another breakthrough in stability has been made by the Zelenay group [180], and their best stable catalyst (PANI-Fe-Co-C), derived from polyaniline (PANI), showed a performance decrease of just 18 μA/cm$^2$ per hour. However, it has a peak power density of only 0.55 W/cm$^2$ (vs 0.91 W/cm$^2$, the best one reported by the Dodelet group, which, however, is less stable) in $H_2$-$O_2$ fuel cell (at 80 °C). Consequently, high-performance and stable non-PGM catalysts have not yet been achieved, and more effort must be made, especially in improving the stability, as currently, none of the best-performing non-PGM catalysts exhibits long-term stability needed for practical applications. Thus, intensive efforts have been done to understand the performance decay mechanisms. Three instability mechanisms have been proposed and mostly discussed: i) demetallation of the catalytic active sites, ii) attack by free radicals and/or $H_2O_2$, iii) micropore flooding.

As mentioned previously, fluorinating the carbonaceous materials is well-known for increasing the hydrophobicity (possibly to improve the mass transport and avoid micropore flooding in fuel cells) and corrosion resistance (possibly to decrease the attack by the free radicals and the demetallation of the catalyst sites from carbon support). Therefore, surface fluorination would have great potential to improve the stability/durability of the non-PGM-based catalysts/cathodes. Nevertheless, most studies were focused on fluorine doping to promote the catalyst performance in ORR half-cell tests, and very less effort has been made to study the fluorination effect on the stability of non-PGM catalysts in PEMFC conditions (in acidic media). Herein, we introduce two representative works about the fluorination effect on the non-PGM catalysts in PEMFC applications.

Wang et al. [195] reported a fluorination strategy to boost the stability of the non-PGM catalyst (Fe/N/C) in PEMFCs. The surface fluorination was realized by covalent-grafting of a trifluoromethylphenyl (Ar-$CF_3$) group on Fe/N/C catalyst. The obtained Fe/N/C−F catalyst shows obvious hydrophobic character, as sown in **Figure 14A,** with a contact angle of ca.

165°, while Fe/N/C material possesses a hydrophilic surface. This property could effectively prevent the water flooding in the Fe/N/C catalyst layer, and thus form many robust channels which promote the gas−liquid two-phase flow, as shown in **Figure 14B.** Further, the Fermi level of the carbon matrix was lowered by the electron-withdrawing property of the Ar-$CF_3$ groups, resulting in an increased reaction energy barrier and decreased carbon oxidation rate. The intrinsic hydrophobic property and the timely removal of the excess water decrease the $H_2O$-involved carbon oxidation rate, which suppresses the demetallation of active sites of the catalyst. This can be demonstrated by **Figure 14C**, where at the cell voltage of 0.5 V, the catalyst with fluorination could deliver a very stable current density of 0.56 A $cm^{-2}$ up to 120 h in an $H_2$-$O_2$ PEMFC. Especially, even at 0.6 V, it can last 100 h with only a 15 % performance loss. This has been also demonstrated by **Figure 14D**, where after a 40-hour operation, the Fe content decreased a little from 1.2 wt% to 1.1 wt% for the fluorinated Fe/N/C catalyst, compared to that of pristine Fe/N/C where Fe content decreased from 1.8 wt% to 0.35 wt%. Besides maintaining the catalytic activity by decreasing carbon corrosion and de-metallization, the creation of robust channels for mass transport (*i.e.,* promoting the gas-fluid two-phase flow) is another important factor in improving the stability of the Fe/N/C catalyst. The concentration overpotential ($\eta_C$) is often used to evaluate the mass transport performance. In **Figure 14E**, it can be seen that with the fuel cell operating time, $\eta_C$ increased for the Fe/N/C catalyst, while decreased for the fluorinated catalyst, demonstrating that, during the durability test, the mass transport performance of the fluorinated cathode is improved. In any case, it is worth noting that though the fluorinated catalyst displayed rather stable currents (~0.6 A $cm^{-2}$ at 0.5 V and ~0.36 A $cm^{-2}$ at 0.6 V), they were much smaller than the initial currents (~1.44 A $cm^{-2}$ at 0.5 V and ~0.08 A $cm^{-2}$ at 0.6 V) for the Fe/N/C catalyst without fluorination. Therefore, more studies need to be performed to understand the effect of fluorination on non-PGM catalysts for PEMFCs.

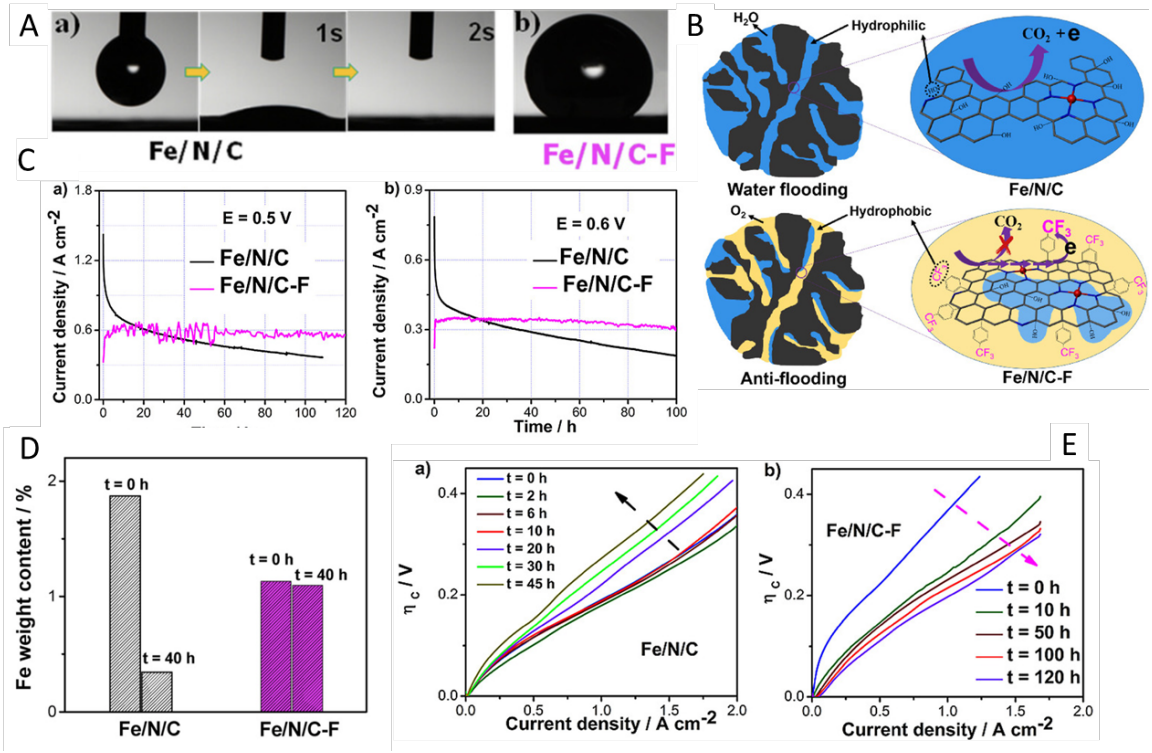


**Figure 14.** (A) Dynamic water contact angles of the Fe/N/C samples with/without fluorination. (B) The hydrophobic and electron-withdrawing trifluoromethylphenyl (Ar-$CF_3$) groups were grafted on the surface of the Fe/N/C catalyst to effectively prevent not only water flooding but also carbon corrosion due to oxidation. (C) Potentiostatic stability test of the Fe/N/C cathodes with/without fluorination in $H_2/O_2$ PEMFC at 0.5 V (a) and 0.6 V (b). The back-pressure: 0.5 bar. Gas flow rate: 200 sccm; membrane: NRE 211; anode: Johnson Matthey 40 wt % Pt/C with 0.4 $mg_{pt}$ $cm^{-2}$ loading; cathode: Fe/N/C-based catalysts with 4.0 mg $cm^{-2}$ loading. (D) Fe weight content of the two catalysts before and after the 40 hours durability test. (E) Evolution of $\eta_C$ with fuel cell operating time for stability test at 0.5 V. Reproduced from [195] with permission from the Chemistry Europe.

Zhang and co-workers [71, 118] have systematically studied the fluorination effect on a series of PGM-free catalysts including i) Black Pearls (BP) with a high microporosity; ii) N-doped Black Pearls (BP-N) to investigate whether the N atoms were affected upon fluorination; iii) MOF_CNx_Ar + $NH_3$ (or shorted as MOF), which is pyrolyzed Zn imidazolate metal-organic framework ZIF-8 (a very popular carbon precursor for fabricating the PGM-free catalysts); iv) the Fe/N/C catalyst [9, 12]. These four catalysts were chosen to be fluorinated because they are the most popular materials discussed in oxygen reduction, and their compositions and structures are progressively changed, finally forming the Fe/N/C type catalyst. The

fluorination was conducted, at room temperature, under a flux of a mixture of 1:1 $F_2/N_2$ gas at atmospheric pressure. The detailed analysis of the fluorine functionalization has been discussed in section 2. Herein, the fluorination effect on the high-performance Fe/N/C catalyst in PEMFCs will be particularly discussed. Note that this representative Fe/N/C catalyst has been studied by the authors for many years regarding its structure, active sites, stability, etc.

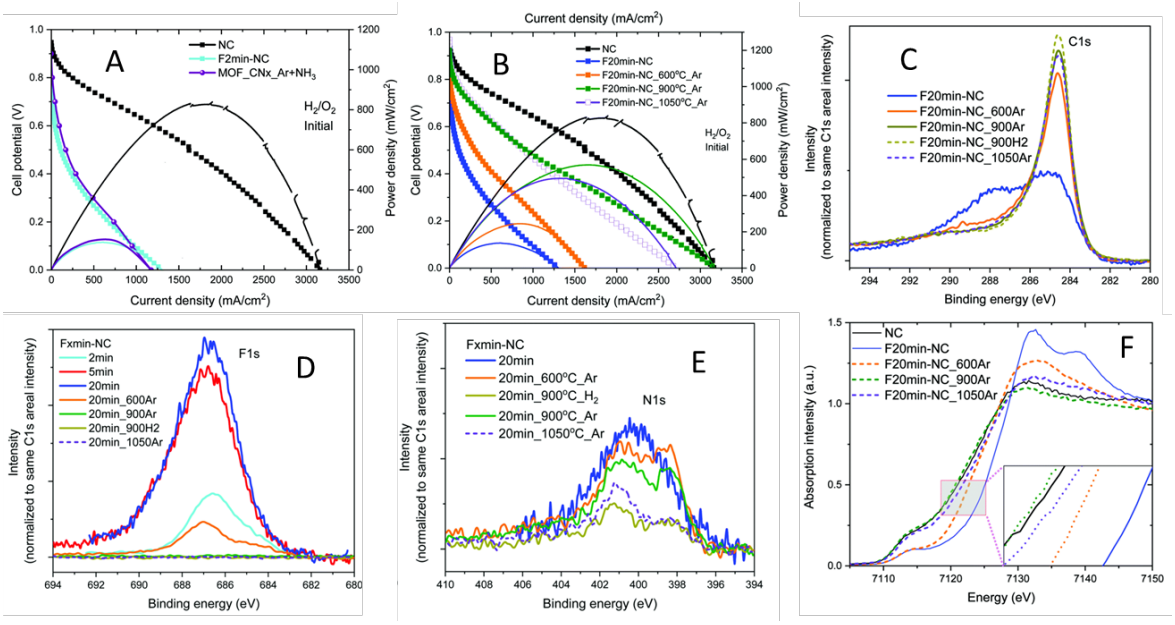


**Figure 15.** (A) $H_2/O_2$ PEMFC test for Fe/N/C catalyst w/o fluorination (where NC is the short name of Fe/N/C catalyst), as well as the MOF_CNx_Ar + $NH_3$ (which is a catalyst without adding iron, *i.e.*, nitrogen-doped carbon catalyst). (B) Initial V-I and power density curves at 80 °C in an $H_2$-$O_2$ PEMFC for NC and fluorinated-NC, as well as heat-treated F20min-NC catalyst at different temperatures in Ar. (C-E) The evolution of the C1s, F1s, and N1s XPS spectra of the F20min-NC catalyst after various heating treatments in $H_2$ or Ar. (F) Normalized Fe K-edge XANES spectra of NC and F20min-NC series catalysts. Reproduced from [118] with permission from the Royal Society of Chemistry.

The initial idea of this work was to verify whether fluorination of the Fe/N/C catalyst can make the carbon support more stable and meanwhile strong enough to hold the Fe sites to avoid demetallation. After the fluorination, unfortunately, the catalyst was totally deactivated. As shown in **Figure 15A**, the fluorinated Fe/N/C (light blue line) has very low activity compared to the pristine Fe/N/C catalyst (black dot line). Interestingly, it is well overlapping the curve of the N-doped carbon (purple line, denoted as $CN_x$ in the figure) without Fe sites. This exactly demonstrated that the FeNx is the main active site of the Fe/N/C catalyst, which is well consistent with previous findings [12]. Further, luckily, the fluorinated catalyst can be

reactivated by heat treatment (**Figure 15B**) even after several years. To understand the detailed reaction that happened on the active sites, the authors conducted a series of characterizations. **Figure 15C-E** shows the evolution of the C1s, F1s, and N1s XPS spectra of fluorinated Fe/N/C after various heat treatments. Obviously, with the heat treatment, the fluorine atoms were gone (**Figure 15D**), and the nitrogen atoms in the catalyst were not affected unless a very high temperature was used such as 1050 °C, with a loss of some nitrogen atoms and simultaneously creating more defect in the carbon support as well (**Figure 15C,E**). Because of the low Fe amounts in the catalysts, the Fe2p XPS analysis could not provide enough chemical information on Fe in the catalytic sites. Thus, the Fe K-edge X-ray absorption near-edge structure (XANES) spectra were performed on Fe/N/C catalysts with/without fluorination, as well as the heat-treated ones obtained in Ar at 600, 900, and 1050°C. As shown in **Figure 15F**, it is obvious that the oxidation state of the iron in pristine Fe/N/C is similar to that of FeO, however, in the F20min-NC catalyst, it is close to that of $Fe_2O_3$. Further, by the combination of the electrochemical evaluation and other physical characterizations of the samples, it demonstrates that when the heating temperature is >= 900 °C, the fluorine atoms are released from the fluorinated catalysts. When the heating treatment temperature is at 600 °C, only partial de-fluorination happens to the catalyst. All these demonstrate that though the fluorination deactivated the Fe/N/C catalyst, the fluorinated catalyst can be reactivated by heat treatment even after several years. This is very important because it can extend the shelf time of the catalyst in practical applications, especially for reliable catalyst manufacture.

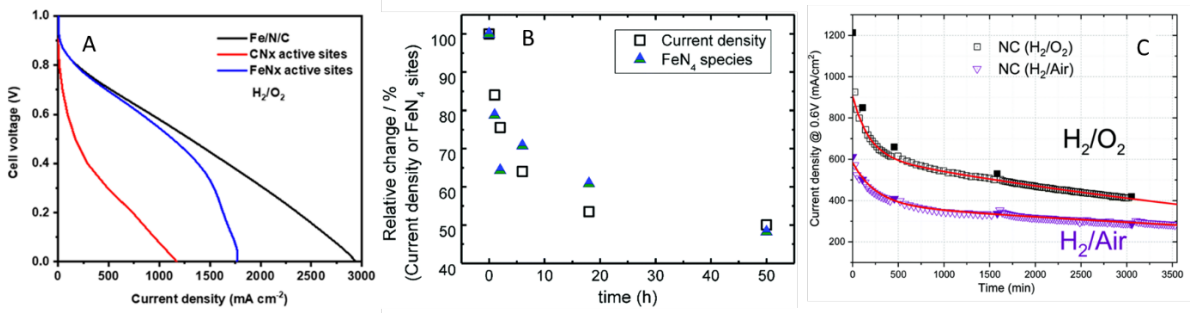


**Figure 16.** (A) Initial fuel cell V-I curves tested at 80 °C in $H_2/O_2$ fuel cell equipped with Fe/N/C cathode catalyst (black line), CNx active sites (red line), and FeNx active sites obtained from the subtraction of CNx active sites from the Fe/N/C polarization curve. (B) Relative changes with fuel cell operating time of: (i) the number of $FeN_4$-like sites (triangles) at the cathode of membrane electrode assemblies (MEAs) using Fe/N/C catalyst and (ii) the current density (at 0.6 V) of the same MEA (squares) in $H_2$-air fuel cells (at 80 °C). The

numbers of $FeN_4$-like active sites were achieved from the combined analysis of the absorption areas in the Mössbauer spectra and the iron amounts determined by neutron activation analysis. (C) Normalized stability behavior at 0.6 V of Fe/N/C catalyst in $H_2$-$O_2$ and $H_2$-air PEM fuel cells (open symbols), with fitted lines based on two exponential decays. Reproduced from [12] with permission from the Elsevier, as well as [13] and [118] with permission from the Royal Society of Chemistry.

Further, combined with the authors' previous study [12-13] regarding the relative contributions of Fe-active sites and the N-doped carbon sites (**Figure 16A**), as well as the loss of the $FeN_x$ (like $FeN_4$) catalytic site content (demonstrated by Mössbauer spectroscopy analysis, **Figure 16B**), the authors propose their stability model for the Fe/N/C catalyst (**Figure 16C**). This model is composed of two exponential decays starting from the fuel cell operation (t=0), *i.e.*, the fast one is due to the demetallation of $FeN_4$ catalytic sites that are located in the micropores of the catalysts, while the second exponential is most probably due to the N-doped carbon sites and the Fe sites located in the mesopores which decay much more slowly.

### 4.3 DFT calculations and thermodynamic calculations

To better understand the fluorination effect on the catalyst performance, understanding the kinetics and thermodynamics of the catalytic reaction is necessary. Recently, density functional theory (DFT) calculations were applied to the active site systems for ORR. However, thermodynamic stability calculations on the same active sites have rarely been reported. The INRS team just pioneered both DFT and thermodynamic calculations on the Fe-based active sites and their fluorinated ones, providing interesting results to understand the instability of the catalyst [196-197].

As mentioned in early sections, some researchers have adopted fluorination strategies to reduce the degradation of the catalysts for ORR in PEM fuel cells. However, the experiments by Zhang and co-workers have revealed that fluorination can poison the $FeN_x$ active sites in the catalyst. This exactly provided a unique opportunity to make a profound study of the nature and the decay mechanisms of the Fe/N/C catalyst in PEM fuel cells. Therefore, to support and deepen the findings from the experimental study, DFT calculation was conducted with optimizations of the ten most possible $FeN_x$ site configurations and two metal-free sites (**Figure 17**). Then F atoms and $F_2$ molecules were introduced to these atomic structures, at different locations, and new DFT optimizations were performed. The binding energies for fluorine (F) atom adsorbed on these structures are shown in the tables of **Figure 17**. When the $FeN_x$ is formed on a single layer of graphene where both sides are accessible, the DFT

simulation demonstrates that the fluorine binds strongly to Fe; and in the case of two fluorine atoms, one F connect with each side of the $FeN_x$ plane will inhibit the activity of the $FeN_x$ sites completely. On the other hand, the multi-graphene layers are more existing in the catalyst than the single-layer graphenes. When considering several graphene layers, it only needs one fluorine atom on top of the graphene layer to poison the $FeN_x$ moiety. This is because the ORR hardly happens between carbon layers. The authors then studied the residual catalytic activity (*i.e.*, in consideration of N-doped carbon with zigzag and armchair structures) after fluorination, for which previously reported DFT simulations indicated a viable catalytic process though with the fact that $O_2$ rarely adsorbs on such structures. For both armchair and zigzag structures, it is demonstrated that the catalytic active site is the carbon atom where an N atom is near it. From DFT calculations, the authors found that fluorination does not poison these catalytic structures (*i.e.*, by F or $F_2$). Therefore, it is demonstrated that the residual ORR catalytic activity (*i.e.*, for fluorinated Fe/N/C catalysts, where the $FeN_x$ active sites are poisoned) is similar to that of the Fe-free catalysts (*e.g.*, carbon with N-doping). Finally, for the regeneration of catalyst activity of fluorinated catalysts, by heat-treatment of them to 900 °C, the authors explained that the fluorine atoms are released from these catalysts upon the heat treatment.

A

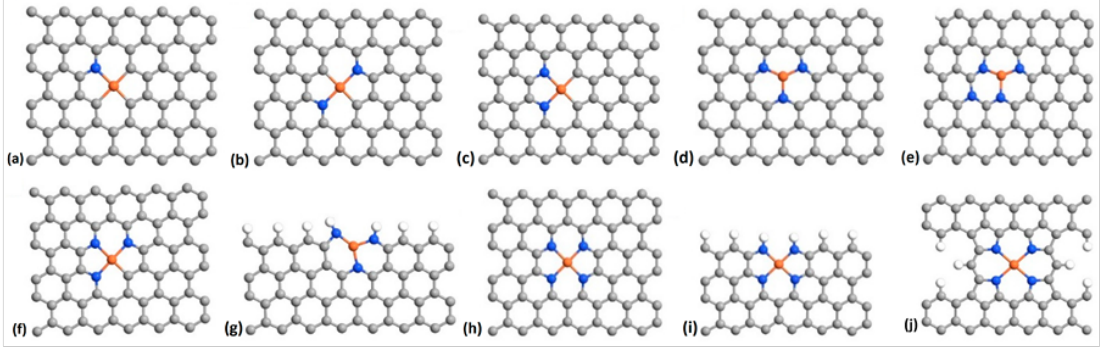


| Structure | Fe–F | F–Fe–F | Fe–$O_2$ |
|---|---|---|---|
| a | −4.27 | −12.10 | −0.84 |
| b | −4.00 | −11.92 | −2.50 |
| c | −3.85 | −11.88 | −2.06 |
| d | −3.94 | −13.04 | −4.60 |
| e | −4.05 | −12.02 | −1.82 |
| f | −4.66 | −12.96 | −3.50 |
| g | −5.89 | −12.94 | −4.55 |
| h | −3.18 | −11.88 | −1.37 |
| i | −2.93 | −10.40 | −1.04 |
| j | −4.56 | −7.88 | −0.71 |

B

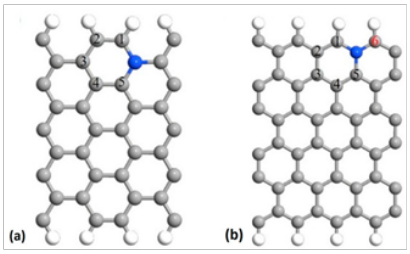


| Structure | Site 1 | Site 2 | Site 3 |
|---|---|---|---|
| Armchair | −2.57 | −2.12 | −2.33 |
| Zigzag | −3.78 | −3.52 | −2.80 |

| Structure | Site 4 | Site 5 |
|---|---|---|
| Armchair | −1.69 | −2.18 |
| Zigzag | −2.36 | −2.97 |

**Figure 17.** (A) DFT optimized ten configurations of $FeN_x$-doped carbon catalysts, and (B) two configurations (armchair and zigzag) of N-doped carbon metal-free catalysts. Color code identification: grey for carbon, blue for nitrogen, and orange for iron. The tables show the Adsorption of F atoms on these structures. Reproduced from [196] with permission from the MDPI.

Thermodynamics is a tool to study the condition or state changes of a substance when its internal energy or temperature changes. An important concept in thermodynamics is the equilibrium state. The precise nature of the equilibrium state is highly dependent on both the character of the system and the constraints imposed on it. Thus, the authors in the same group conducted the thermodynamic calculations to reveal the thermodynamic stability of the $FeN_4$ catalytic active sites with and without fluorination, in consideration of the acidic medium and operating temperature in real PEMFCs. Again, the two most popular $FeN_4$-based catalytic sites as mentioned above have been calculated, in an acidic condition (pH ~ 0) at 298 and 353 K to

mimic the real fuel cell environment (**Figure 18**). The related thermodynamic stability ($K_c$ values) are presented in the Tables in **Figure 18**. It reveals that the $K_c$ values change over a wide range, depending on the number (m=0, 1, 2, where 0 is the case of non-fluorinated, while m=1 and 2 is the condition of adding one or two fluorine atoms on the active sites) of F-atoms that are connecting to the iron. In the condition of non-fluorinated catalysts, the chemical stability of the 1.10-phenanthroline-like sites is much higher than that of the porphyrin-like sites. After fluorination, porphyrin-like $FeN_4F[H_{29}C_{112}F_{32}]$ (with one fluorine atom in the active site) and 1,10-phenanthroline-like $FeN_{(2+2)}F_2[C_{60}H_{15}F_{21}]_2$ sites (with two fluorine atoms) are the most chemically stable ones among fluorinated electrocatalysts. This indicates that the fluorination of these two active sites increases the catalyst's chemical resistance to acid iron leaching. On the other hand, it should be noticed that the catalyst is under dynamic conditions, where Fe ions could leave the system (e.g., due to the exchange for $H^+$ in the proton exchange membrane, leaving the cathode with the flow of $H_2O$ in the fuel cell system). Therefore, according to Le Chatelier's principle, if the equilibrium between the Fe ions in and out of the active sites could not be established, it can cause the progressive demetallation of the electrocatalytic sites. All these findings are consistent with their experimental results and DFT calculations. The next step is to develop new strategies to take full use of fluorination to stabilize the catalysts.

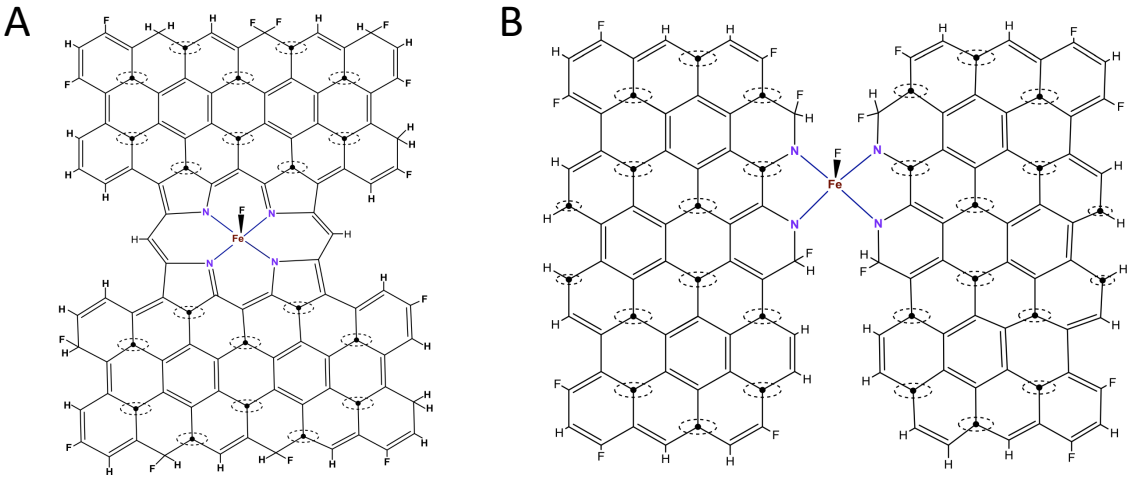


**Thermodynamic data on iron acid leaching of the modelled fluorinated and non-fluorinated porphyrin-like active sites.**

| Modelled active site | Reaction of iron acid leaching | $\Delta_r H^0_{298}$, kJ mol$^{-1}$ | $\Delta_r S^0_{298}$, J mol$^{-1}$K$^{-1}$ | $K_c$ at temperature T/K | |
|---|---|---|---|---|---|
| | | | | 298 | 353 |
| $FeN_4[H_{29}C_{112}F_{32}]$ | Eq. 2 | 1.3 | −117.2 | $4.5 \times 10^{-7}$ | $4.8 \times 10^{-7}$ |
| $FeN_4F[H_{29}C_{112}F_{32}]$ | Eq. 1 | −42.7 | −311.2 | $1.7 \times 10^{-9}$ | $1.2 \times 10^{-10}$ |
| $FeN_4F_2[H_{29}C_{112}F_{32}]$ | Eq. 1 | −50.6 | −325.0 | $7.8 \times 10^{-9}$ | $3.2 \times 10^{-10}$ |
| $FeN_4C_{12}$ (non-fluorinated "zig-zag" electrocatalyst)* | – | 3.7* | −123.3* | $8.1 \times 10^{-8}$ * | $1.0 \times 10^{-7}$ * |

**Thermodynamic data on iron acid leaching of the modelled fluorinated and non-fluorinated 1,10-phenathroline-like active sites.**

| Modelled active site | Reaction of iron acid leaching | $\Delta_r H^0_{298}$, kJ mol$^{-1}$ | $\Delta_r S^0_{298}$, J mol$^{-1}$K$^{-1}$ | $K_c$ at temperature T/K | |
|---|---|---|---|---|---|
| | | | | 298 | 353 |
| $FeN_{(2+2)}[C_{60}H_{15}F_{21}]_2$ | Eq. 4 | 7.7 | −122.2 | $1.9 \times 10^{-8}$ | $3 \times 10^{-8}$ |
| $FeN_{(2+2)}F[C_{60}H_{15}F_{21}]_2$ | Eq. 3 | −65.3 | −324.2 | $3.2 \times 10^{-6}$ | $5.3 \times 10^{-8}$ |
| $FeN_{(2+2)}F_2[C_{60}H_{15}F_{21}]_2$ | Eq. 3 | −45.9 | −347.0 | $8.3 \times 10^{-11}$ | $4.6 \times 10^{-12}$ |
| $FeN_{(2+2)}$/C (non-fluorinated "armchair" electrocatalyst)* | – | 5.3* | −121.0* | $5.6 \times 10^{-8}$ * | $8.0 \times 10^{-8}$ * |

**Figure 18.** Molecular models for the fluorinated catalysts: (A) the porphyrin-like $FeN_4$/C-active sites and (B) phenanthroline-like $FeN_{(2+2)}$/C active sites, as well as their thermodynamic data in consideration of the active sites with and without fluorination. Reproduced from [197] with permission from the ECS.

## 5. Perspectives

In summary, fluorination can play an important role in energy conversion and storage technologies. Specifically, in this review, we focused on the discussion of the fluorination effects on the electrocatalysts for low-temperature fuel cells. We first addressed the various fluorination methods and their benefits to the property of the materials, including polarity and surface tension, changes in the pore size distribution, co-doping effect with fluorine, as well as bond formation caused by the fluorination. Then, we summarized recent advances in the development of various fluorinated electrocatalysts for ORR in fuel cells, including noble and non-noble metal catalysts, where fluorination plays a key role in tuning the

hydrophobicity/hydrophilicity property of the catalyst layers and affects the activity and stability/durability/lifetime of the catalysts. We believe that this review provides insights into fluorination for the community of not only fuel cells but also other energy conversion and storage systems. Several perspectives are provided for the future application of fluorination and its study in fuel cells:

1. How well use the fluorination strategy to tailor the bonding, structure and property of the materials used in fuel cells, including carbonaceous material (SSA, crystallinity, doping, etc.) and the metal active sites in the catalysts, in order either to keep them or to change them favorably for fuel cell applications. Especially, the electronic properties and C-F bonding can be well-tailored, by taking advantage of co-doping other heteroelements (N, S, P) with fluorine. Co-doping with fluorine is underused according to its versatility.
2. The precise characterization and study of the materials on the electronic properties and C-F bonding by fluorination, as well as the real active sites for ORR in fuel cells are necessary, via various advanced characterization techniques, such as XPS, IR, NMR, EPR, $N_2$ sorption, as well as aberration-corrected high-angle annular dark-field scanning transmission electron microscopy (AC-corrected HAADF-STEM), synchrotron-based X-ray absorption spectroscopy (XAS) and imaging, and so on.
3. Understanding the structure-property relationship and the reaction mechanisms of the fluorinated materials especially their activity and degradation during fuel cell operation is critical. The well-known *in situ/operando* techniques include XAS, electrochemical impedance spectroscopy (EIS), and real-time mass spectrometry (*e.g.*, stability study of materials by monitoring $CO_2$ evolution originated from the electro-oxidation of carbon).
4. DFT and thermodynamic simulations are powerful tools for revealing the reaction mechanism of the catalysts and predicting the potential active species. However, accurate assessments of the catalytic active centers, especially in consideration of the real reaction environment (*e.g.*, solid/liquid/gas, pH value of the reaction, temperature, employed pressure, etc.), are still needed for in-depth study. It is also suggested to combine the experimental results, *ex-/in-situ* characterizations, and the theoretical modelling all together to better reveal the active sites and their reaction mechanism.
5. Fluorination is well accepted for having great potential to prolong the lifetime of the materials, new protocols need to be identified to fast screen and reveal the fluorination effect on the lifetime of the materials.

6. Fluorination of non-PMG catalyst was blocking all $FeN_x$ sites of the catalyst by forming either F-$FeN_x$ or F-$FeN_x$-F bonds but after several months, and even after a few years, when a heat treatment is carried out, the catalyst can be regenerated and recover its high activity. Up to now, 70-75% activity back is achieved. The sequence protection (Fluorination)/Reactivation (Heating) allows for increasing the shelf-life of non-PGM catalysts[118]. Nevertheless, C-F bonds break before the Fe-F bonds, so it is not possible to thermally obtain $FeN_x$ sites free of F without first removing all C-F bonds that are suspected to protect the carbon support from oxidation. Therefore, to improve fuel cell performances, it is suggested that the catalyst active sites should be added after the fluorination process of the carbon support. With this two-step process, high-performance catalysts with enhanced stability may be achieved.
7. The addition of chemical protection to the active sites before fluorination (to avoid any poisoning of the active sites by fluorination because of the strong interaction of fluorine with metal than carbon), followed by the removal of that chemical protection after fluorination (*i.e.*, to expose the high active sites to the fluorinated carbon support to make the entire catalyst not only highly active but also highly stable to sustain the attack by $H_2O_2$/free radicals in fuel cells). Several studies have shown that $FeN_x$ ORR sites in acid can be deactivated by pseudohalide (*e.g.,* $SCN^-$ or $CN^-$), and then regenerated in a KOH solution**.**

The present paper aims to give the strategy to tailor the fluorination according to the characteristics of the carbonaceous material (SSA, crystallinity, doping, presence of catalyst) in order either to keep them or to change them favorably.

We believe that the data would be useful for the community of the fuel cells but also for other applications where the electronic properties and C-F bonding must be tailored thanks to co-doping with fluorine and other heteroelements (*e.g.*, N, S, P). The co-doping with fluorine is underused according to its versatility.

Overall, with the continuous research in this promising field, we believe that the good use of the fluorination technique could significantly leverage the wide application of various materials in electrochemical energy conversion and storage devices, to address the climate change and energy shortage issues that we are facing.

**Acknowledgements**

M. Dubois and M. Colin acknowledge I-Site CAP2025, Université Clermont Auvergne, and Clermont Auvergne Métropole for support via the Académie CAP20-25. G. Zhang acknowledges École de Technologie Supérieure (ÉTS), Marcelle-Gauvreau Engineering Research Chair program and CAP 20-25 Visiting Scholar Fellowship.

Marian Chatenet, Sandrine Berthon-Fabry, Yasser Ahmad, Katia Guérin, and Marc Dubois acknowledge the French National Research Agency programme, (ANR-14-CE05-0047 project CORECAT) for funding a part of this work.

Received: ((will be filled in by the editorial staff))

Revised: ((will be filled in by the editorial staff))

Published online: ((will be filled in by the editorial staff))

Marian Chatenet obtained a PhD in Electrochemistry (Grenoble-INP, 2000). After a post-doctorate (University of Minnesota), he became associate professor (2002) and professor (2011) in Grenoble-INP to study electrocatalysis and activity/durability of low-temperature fuel cells/electrolyzers. Best young scientist in Electrochemistry (French Chemical Society, 2009), he received the Oronzio and Niccolò De Nora Foundation Prize on Applied Electrochemistry (International Society of Electrochemistry, 2010), and the Electrocatalysis Distinguished Merit Award (Springer-Nature, 2018). Co-chair the "Mobility Applications" axis of the Hydrogen Federation of CNRS and Editor for J. Power Sources, he published 180+ papers, 9 patent and 250+ (inter)national conferences (50+ invited).

Sandrine BERTHON-FABRY obtained her Ph.D. in 1994 from University of Bordeaux, France in Chemical sciences specialized in materials. She got a post doctorate position at CSIC-ICMAB in Barcelona, Spain, in 1995. She joined the PERSEE centre of MINES Paris-PSL, France in 1996 as researcher. Her researches deal with materials for energy conversion, storage and conservation. It covers the elaboration, characterization of (nano)materials based on carbon, metal oxide, organic-inorganic composites applied to PEMFC, lithium batteries, supercapacitors or as superinsulating materials. She has been involved in more than 25 R&D projects and has authored about 180 scientific publications (articles, patents, conferences).

Yasser Ahmad works at Fahad Bin Sultan University in Tabuk (KSA). In 2013, he earned his Ph.D. from Clermont Auvergne University in France. His research focuses on the synthesis of functional (nano)carbons under a fluorinated environment, their characterization and their commercialization for application in lithium batteries and fuel cells, among other energy storage technologies. The majority of syntheses are focused on creating those materials via heterogeneous gas/solid reactions in a variety of fluorine atmospheres ($F_2$, HF, $TbF_4$, $XeF_2$, etc.).

Katia Guérin Araujo da Silva is an Associate Professor of the Clermont Auvergne University. After recieving the title of engineer from the ENSCPB school, she received her Ph.D. in chemical physics at Bordeaux University in 1999. She worked on the lithium-ion insertion mechanism into graphite and hard carbons through solid state NMR and Raman spectroscopies. Her research activities are now focused on solid-gas fluorine chemistry to discover new materials usable mainly in electrochemical energy storage materials in batteries, fuel cells and supercapacitors.

Prof. **Gaixia Zhang** is a Marcelle-Gauvreau Engineering Research Chair Professor at École de Technologie Supérieure (ÉTS), University of Quebec, Montréal, Canada. She received her Ph.D. degree from Polytechnique Montréal, and then continued her research at Western University and INRS, Canada. Her research interests focus on advanced materials (catalysts, electrodes and electrolytes) for sustainable energy conversion and storage applications, including fuel cells, batteries, hydrogen production, and $CO_2$ reduction. She is also interested in interface and device engineering, as well as in-situ characterizations and theoretical simulations.

Marc Dubois is full professor at the Clermont Auvergne University since 2008. He has a strong experience in the inorganic fluorine chemistry and chemistry of carbonaceous, fluoride and (oxi)fluoride materials. From his thesis work and a postdoctoral position at *Institut des Matériaux de Nantes*, to now at the *Institut de Chimie de Clermont-Ferrand* (UMR CNRS 6296), materials for energy storage are in the heart of its research activities. Syntheses are mainly centered on the preparation of those materials using heterogeneous gas/solid reaction under different fluorine atmospheres ($F_2$, HF, $XeF_2$, …). He has worked in areas related to fluorinated materials, in particular fluorinated (nano)carbons in the domains of energy, lubrication and gas sensors.

References

[1]. Y. Manoharan, S. E. Hosseini, B. Butler, H. Alzhahrani, B. T. F. Senior, T. Ashuri, J. Krohn, *Appl. Sci.* **2019**, 9, 2296.
[2]. Y. Guo, F. Pan, W. Chen, Z. Ding, D. Yang, B. Li, P. Ming, C. Zhang, *Electrochem. Energ. Rev.* **2021**, 4, 67.
[3]. Z. Shang, R. Wycisk, P. Pintauro, *Energies* **2021**, 14, 6709.
[4]. Y. Ahmad, S. Berthon-Fabry, M. Chatenet, G. Monier, M. Dubois, K. Guerin, *J. Fluor. Chem.* **2020**, 238, 109633.
[5]. H. Niu, C. Xia, L. Huang, S. Zaman, T. Maiyalagan, W. Guo, B. You, B. Y. Xia, *Chinese J. Catal.* **2022**, 43, 1459.
[6]. L. Du, G. Zhang, S. Sun, *Automotive Innovation* **2021**, 4, 131.
[7]. X. Yang, G. Zhang, L. Du, J. Zhang, F.-K. Chiang, Y. Wen, X. Wang, Y. Wu, N. Chen, S. Sun, *ACS Appl. Mater. Interfaces* **2020**, 12, 13739.
[8]. M. Lefèvre, E. Proietti, F. Jaouen, J.-P. Dodelet, *Science (New York, N.Y.)* **2009**, 324, 71.
[9]. E. Proietti, F. Jaouen, M. Lefèvre, N. Larouche, J. Tian, J. Herranz, J.-P. Dodelet, *Nat. Commun.* **2011**, 2, 416.
[10]. K. Parvez, S. Yang, Y. Hernandez, A. Winter, A. Turchanin, X. Feng, K. Müllen, *ACS Nano* **2012**, 6, 9541.
[11]. J. Li, S. Brüller, D. C. Sabarirajan, N. Ranjbar-Sahraie, M. T. Sougrati, S. Cavaliere, D. J. Jones, I. V. Zenyuk, A. Zitolo, F. Jaouen, *ACS Appl. Energy Mater.* **2019**.
[12]. G. Zhang, R. Chenitz, M. Lefèvre, S. Sun, J.-P. Dodelet, *Nano Energy* **2016**, 29, 111.
[13]. R. Chenitz, U. I. Kramm, M. Lefèvre, V. Glibin, G. Zhang, S. Sun, J.-P. Dodelet, *Energy Environ. Sci.* **2018**, 11, 365.
[14]. J. Weiss, H. Zhang, P. Zelenay, *J. Electroanal. Chem.* **2020**, 875, 114696.
[15]. S. Zeng, S. Wang, H. Zhuang, B. Lu, C. Li, Y. Wang, G. Wang, *Electrochim. Acta* **2022**, 420, 140460.
[16]. Y. Sim, S. J. Kim, G. Janani, Y. Chae, S. Surendran, H. Kim, S. Yoo, D. C. Seok, Y. H. Jung, C. Jeon, J. Moon, U. Sim, *Appl. Surf. Sci.* **2020**, 507, 145157.
[17]. Y. L. F. Musico, N. Kakati, M. F. M. Labata, J. D. Ocon, P.-Y. A. Chuang, *Mater. Chem. Phys.* **2019**, 236, 121804.
[18]. A. Alashkar, A. Al-Othman, M. Tawalbeh, M. Qasim, *Membranes* **2022**, 12, 178.
[19]. R. Vinodh, R. Atchudan, H.-J. Kim, M. Yi, *Polymers* **2022**, 14, 300.
[20]. T. K. Maiti, J. Singh, P. Dixit, J. Majhi, S. Bhushan, A. Bandyopadhyay, S. Chattopadhyay, *Chem. Eng. J. Adv.* **2022**, 12, 100372.
[21]. M. Mariani, A. Basso Peressut, S. Latorrata, R. Balzarotti, M. Sansotera, G. Dotelli, *Energies* **2021**, 14, 8387.
[22]. L. Borchardt, M. Oschatz, S. Kaskel, *Mater. Horizons* **2014**, 1, 157.
[23]. N. Sharma, M. Dubois, K. Guérin, V. Pischedda, S. Radescu, *Energy Technol.* **2021**, 9, 2000605.
[24]. M. Adamska, U. Narkiewicz, *J. Fluor. Chem.* **2017**, 200, 179.
[25]. X. Li, H. Zhang, C. Liu, J. Qiao, X. Zhou, *Microporous and Mesoporous Mater.* **2021**, 310, 110650.
[26]. S. Martins, F. Withers, M. Dubois, M. Craciun, S. Russo, *New J. Phys.* **2013**, 15, 033024.
[27]. F. Withers, S. Russo, M. Dubois, M. F. Craciun, *Nanoscale Res. Lett.* **2011**, 6, 526.
[28]. F. Withers, T. H. Bointon, M. Dubois, S. Russo, M. F. Craciun, *Nano. Lett.* **2011**, 11, 3912.

[29]. W. Zhang, L. Moch, M. Dubois, K. Guérin, J. Giraudet, F. Masin, A. Hamwi, *J. Nanosci. Nanotechnol.* **2009**, 9, 4496.
[30]. S. Zhou, S. D. Sherpa, D. W. Hess, A. Bongiorno, *J. Phys. Chem. C.* **2014**, 118, 26402.
[31]. M. Mar, M. Dubois, K. Guérin, N. Batisse, B. Simon, P. Bernard, *Carbon* **2019**, 141, 6.
[32]. W. Zhang, M. Dubois, K. Guérin, P. Bonnet, E. Petit, N. Delpuech, D. Albertini, F. Masin, A. Hamwi, *Carbon* **2009**, 47, 2763.
[33]. K. Guérin, M. Dubois, A. Houdayer, A. Hamwi, *J. Fluor. Chem.* **2012**, 134, 11.
[34]. Y. Ahmad, K. Guérin, M. Dubois, W. Zhang, A. Hamwi, *Electrochim. Acta* **2013**, 114, 142.
[35]. W. Zhang, M. Dubois, K. Guérin, A. Hamwi, J. Giraudet, F. Masin, *J. Solid State Chem.* **2008**, 181, 1915.
[36]. M. Dubois, K. Guérin, J. P. Pinheiro, Z. Fawal, F. Masin, A. Hamwi, *Carbon* **2004**, 42, 1931.
[37]. J. Giraudet, M. Dubois, K. Guérin, A. Hamwi, F. Masin, *J. Phys. Chem. Solids* **2006**, 67, 1100.
[38]. C. Matei Ghimbeu, K. Guerin, M. Dubois, S. Hajjar-Garreau, C. Vix-Guterl, *Carbon* **2015**, 84, 567.
[39]. W. Zhang, K. Guérin, M. Dubois, A. Houdayer, F. Masin, A. Hamwi, *Carbon* **2008**, 46, 1017.
[40]. Y. Ahmad, M. Dubois, K. Guérin, A. Hamwi, W. Zhang, *Carbon* **2015**, 94, 1061.
[41]. Y. Ahmad, E. Disa, M. Dubois, K. Guérin, V. Dubois, W. Zhang, P. Bonnet, F. Masin, L. Vidal, D. A. Ivanov, A. Hamwi, *Carbon* **2012**, 50, 3897.
[42]. M. Dubois, J. Giraudet, K. Guérin, A. Hamwi, Z. Fawal, P. Pirotte, F. Masin, *J. Phys. Chem. B* **2006**, 110, 11800.
[43]. V. Cardoso, D. M. Correia, C. Ribeiro, M. Fernandes, S. Lanceros-Méndez, *Polym.* **2018**, 10, 161.
[44]. S. Al-Gharabli, W. Kujawski, Z. A. El-Rub, E. M. Hamad, J. Kujawa, *J. Memb. Sci.* **2018**, 556, 214.
[45]. J. Son, Y. Kim, J.-K. Lee, S. K. Kim, W. Koo, J. G. Yoon, J. Y. Yang, *J. Fluor. Chem.* **2019**, 227, 109388.
[46]. V. F. Cardoso, D. M. Correia, C. Ribeiro, M. M. Fernandes, S. Lanceros-Méndez, *Polym.* **2018**, 10.
[47]. Q. Guo, Y. Huang, M. Xu, Q. Huang, J. Cheng, S. Yu, Y. Zhang, C. Xiao, *J. Membr. Sci.* **2022**, 664, 121115.
[48]. J. Parmentier, S. Schlienger, M. Dubois, E. Disa, F. Masin, T. A. Centeno, *Carbon* **2012**, 50, 5135.
[49]. W. Na, J. Kim, Y. K. Kim, S. G. Kim, J. Jang, *Carbon* **2020**, 165, 185.
[50]. F. A. Viva, G. A. Olah, G. K. S. Prakash, *Int. J. Hydrog. Energy.* **2017**, 42, 15054.
[51]. A. Tristan, R. Chattot, F. Maillard, L. Dubau, Y. Ahmad, N. Batisse, M. Dubois, K. Guérin, F. Labbé, R. Metkemeijer, S. Berthon-Fabry, M. Chatenet, *J. Electrochem. Soc.* **2018**, 165, F3346.
[52]. D. E. Glass, V. Galvan, M. Iulliucci, G. K. S. Prakash, *J. Power Sources* **2022**, 542, 231725.
[53]. L. F. Velasco, K. H. Kim, Y.-S. Lee, P. Lodewyckx, *Front. Chem.* **2021**, 8, 593756.
[54]. T. Van Nguyen, A. Ahosseini, X. Wang, V. Yarlagadda, A. Kwong, A. Z. Weber, P. Deevanhxay, S. Tsushima, S. Hirai, *J. Electrochem. Soc.* **2015**, 162, F1451.
[55]. E. M. Can, A. Mufundirwa, P. Wang, S. Iwasaki, T. Kitahara, H. Nakajima, M. Nishihara, K. Sasaki, S. M. Lyth, *J. Power Sources* **2022**, 548, 232098.

[56]. R. S. Bakdash, I. H. Aljundi, C. Basheer, I. Abdulazeez, A. A. Al-Saadi, *Global Chall.* **2021**, 5, 2000124.
[57]. K. Kinoshita, *J. Electrochem. Soc.* **1990**, 137, 845.
[58]. D. Banham, S. Ye, K. Pei, J.-i. Ozaki, T. Kishimoto, Y. Imashiro, *J. Power Sources* **2015**, 285, 334.
[59]. T. Asset, P. Atanassov, *Joule* **2020**, 4, 33.
[60]. A. Zitolo, V. Goellner, V. Armel, M.-T. Sougrati, T. Mineva, L. Stievano, E. Fonda, F. Jaouen, *Nat. Mater.* **2015**, 14, 937.
[61]. D. Guo, R. Shibuya, C. Akiba, S. Saji, T. Kondo, J. Nakamura, *Science (New York, N.Y.)* **2016**, 351, 361.
[62]. F. Jaouen, M. Lefèvre, J.-P. Dodelet, M. Cai, *J. Phys. Chem. B* **2006**, 110, 5553.
[63]. J. Li, S. Ghoshal, W. Liang, M.-T. Sougrati, F. Jaouen, B. Halevi, S. McKinney, G. McCool, C. Ma, X. Yuan, Z.-F. Ma, S. Mukerjee, Q. Jia, *Energy Environ. Sci.* **2016**, 9, 2418.
[64]. Y. Wang, S. Berthon-Fabry, *Electrocatalysis* **2021**, 12, 78.
[65]. F. Jaouen, E. Proietti, M. Lefèvre, R. Chenitz, J.-P. Dodelet, G. Wu, H. T. Chung, C. M. Johnston, P. Zelenay, *Energy Environ. Sci.* **2011**, 4, 114.
[66]. J. Pampel, T.-P. Fellinger, *Adv. Energy Mater.* **2016**, 6, 1502389.
[67]. A. Serov, M. H. Robson, K. Artyushkova, P. Atanassov, *Appl. Catal. B.* **2012**, 127, 300.
[68]. Y. Zhou, Y. Yu, D. Ma, A. C. Foucher, L. Xiong, J. Zhang, E. A. Stach, Q. Yue, Y. Kang, *ACS Catal.* **2021**, 11, 74.
[69]. Y. Wang, M. J. Larsen, S. Rojas, M.-T. Sougrati, F. Jaouen, P. Ferrer, D. Gianolio, S. Berthon-Fabry, *J. Power Sources* **2021**, 514, 230561.
[70]. S. Berthon-Fabry, L. Dubau, Y. Ahmad, K. Guerin, M. Chatenet, *Electrocatalysis* **2015**, 6, 521.
[71]. G. Zhang, M. Colin, X. Yang, S. Sun, J.-P. Dodelet, M. Dubois, *Appl. Surf. Sci.* **2022**, 577, 151721.
[72]. K. Gong, F. Du, Z. Xia, M. Durstock, L. Dai, *Science (New York, N.Y.)* **2009**, 323, 760.
[73]. S. Wang , E. Iyyamperumal , A. Roy, Y. Xue, D. Yu, L. Dai, *Angew. Chem. Int. Ed.* **2011**, 50, 11756.
[74]. S. Akula, B. Balasubramaniam, P. Varathan, A. K. Sahu, *ACS Appl. Energy Mater.* **2019**, 2, 3253.
[75]. R. Qin, Q. Qian, Y. Liu, A. Ou, Y. Li, X. Liu, X. Liu, X. Wang, *J. Phys. Chem. C.* **2019**, 123, 16439.
[76]. Q. He, J. Jiang, J. Zhu, Z. Pan, C. Li, M. Yu, J. Key, P. K. Shen, *J. Power Sources* **2020**, 448, 227568.
[77]. P. Zhu, J. Gao, X. Chen, S. Liu, *Int. J. Hydrog. Energy.* **2020**, 45, 9512.
[78]. F. Liu, Z. Li, Y. Li, Y. Feng, W. Feng, *Carbon* **2021**, 181, 9.
[79]. Y. Nie, S. Wang, Y. Lin, W. Lai, W. Weng, D. Tang, *Spectrochim. Acta A Mol. Biomol.* **2021**, 250, 119231.
[80]. J. Zhu, H. Chu, J. Shen, C. Wang, Y. Wei, *J. Colloid Interface Sci.* **2021**, 586, 683.
[81]. J. Wang, X. Hu, H. Ding, X. Huang, M. Xu, Z. Li, D. Wang, X. Yan, Y. Lu, Y. Xu, Y. Chen, P. C. Morais, Y. Tian, R.-Q. Zhang, H. Bi, *ACS Appl. Mater. Interfaces* **2019**, 11, 18203.
[82]. H. Wang, J. Sun, J. Wang, L. Jiang, H. Liu, *J. Mater. Res. Technol.* **2021**, 13, 962.
[83]. X. Li, Y. Li, R. Qin, F. Huang, X. Wang, X. Liu, *Ind. Eng. Chem. Res.* **2021**, 60, 875.
[84]. T. Nakajima, Y. Matsuo, *Carbon* **1994**, 32, 469.
[85]. L. Pu, Y. Ma, W. Zhang, H. Hu, Y. Zhou, Q. Wang, C. Pei, *RSC Adv.* **2013**, 3, 3881.
[86]. O. Jankovský, P. Šimek, D. Sedmidubský, S. Matějková, Z. Janoušek, F. Šembera, M. Pumera, Z. Sofer, *RSC Adv.* **2014**, 4, 1378.

[87]. Z. Wang, J. Wang, Z. Li, P. Gong, X. Liu, L. Zhang, J. Ren, H. Wang, S. Yang, *Carbon* **2012**, 50, 5403.
[88]. S. Yan, J. Zhao, Y. Yuan, S. Liu, Z. Huang, Z. Chen, D. Jiang, W. Zhao, *RSC Adv.* **2013**, 3, 21869.
[89]. M. Mar, M. Dubois, K. Guérin, N. Batisse, B. Simon, P. Bernard, *J. Fluor. Chem.* **2019**, 227, 109369.
[90]. F. Wang, L. Wang, Q. Xue, *Carbon* **2016**, 96, 411.
[91]. C. Struzzi, H. Sezen, M. Amati, L. Gregoratti, N. Reckinger, J. F. Colomer, R. Snyders, C. Bittencourt, M. Scardamaglia, *Appl. Surf. Sci.* **2017**, 422, 104.
[92]. H. Yamamoto, K. Matsumoto, Y. Matsuo, Y. Sato, R. Hagiwara, *Dalton Trans.* **2020**, 49, 47.
[93]. A. M. Panich, *Synth. Met.* **1999**, 100, 169.
[94]. T. Mallouk, B. L. Hawkins, M. P. Conrad, K. Zilm, G. E. Maciel, N. Bartlett, R. J. Gillespie, P. Day, *Philos. Trans. Royal Soc.* **1985**, 314, 179.
[95]. J. Giraudet, M. Dubois, A. Hamwi, W. E. Stone, P. Pirotte, F. Masin, *J. Phys. Chem. B* **2005**, 109, 175.
[96]. J. Giraudet, M. Dubois, K. Guérin, C. Delabarre, A. Hamwi, F. Masin, *J. Phys. Chem. B.* **2007**, 111, 14143.
[97]. H. Touhara, F. Okino, *Carbon* **2000**, 38, 241.
[98]. W. Zhang, M. Dubois, K. Guérin, P. Bonnet, H. Kharbache, F. Masin, A. P. Kharitonov, A. Hamwi, *Phys. Chem. Chem. Phys.* **2010**, 12, 1388.
[99]. Y. Sato, K. Itoh, R. Hagiwara, T. Fukunaga, Y. Ito, *Carbon* **2004**, 42, 3243.
[100]. S. Kumar, M. B. Gawande, J. Kopp, S. Kment, R. S. Varma, R. Zbořil, *ChemSusChem* **2020**, 13, 5135.
[101]. J. Zhang, L. Dai, *Angew. Chem. Int. Ed.* **2016**, 55, 13296.
[102]. D. Zhu, J. Yuan, T. Wang, Y. Dai, Y. Peng, W. Li, A. Li, J. Zhang, *J. Power Sources* **2022**, 551, 232188.
[103]. X. Tong, X. Zhan, Z. Gao, G. Zhang, Y. Xie, J. Tian, H. Ranganathan, D. Li, J. P. Claverie, S. Sun, *Chem. Commun.* **2022**, 58, 11519.
[104]. X. Zhan, X. Tong, M. Gu, J. Tian, Z. Gao, L. Ma, Y. Xie, Z. Chen, H. Ranganathan, G. Zhang, S. Sun, *Nanomaterials* **2022**, 12, 1141.
]105]. X. Tong, M. Cherif, G. Zhang, X. Zhan, J. Ma, A. Almesrati, F. Vidal, Y. Song, J. P. Claverie, S. Sun, *ACS Appl. Mater. Interfaces* **2021**, 13, 30512.
[106]. Q. Wei, X. Yang, G. Zhang, D. Wang, L. Zuin, D. Banham, L. Yang, S. Ye, Y. Wang, M. Mohamedi, S. Sun, *Appl. Catal. B.* **2018**, 237, 85.
[107]. Q. Wei, M. Cherif, G. Zhang, A. Almesrati, J. Chen, M. Wu, N. Komba, Y. Hu, T. Regier, T.-K. Sham, F. Vidal, S. Sun, *Nano Energy* **2019**, 62, 700.
[108]. Z.-H. Sheng, H.-L. Gao, W.-J. Bao, F.-B. Wang, X.-H. Xia, *J. Mater. Chem.* **2012**, 22, 390.
[109]. J. Zhang, J. Zhang, F. He, Y. Chen, J. Zhu, D. Wang, S. Mu, H. Y. Yang, *Nano-Micro Lett.* **2021**, 13, 65.
[110]. Y. Shao, Z. Jiang, Q. Zhang, J. Guan, *ChemSusChem* **2019**, 12, 2133.
[111]. R. Ma, G. Lin, Y. Zhou, Q. Liu, T. Zhang, G. Shan, M. Yang, J. Wang, *npj Comput. Mater.* **2019**, 5, 78.
[112]. M. Dubois, K. Guérin, A. Hamwi, A. Vinogradov, 9 - Nature of C–F Bonds in Fluorinated Carbons. In *New Fluorinated Carbons: Fundamentals and Applications*, Boltalina, O. V., Nakajima, T., Eds. Elsevier: Boston, 2017; pp 215.
[113]. M. Dubois, K. Guérin, Y. Ahmad, N. Batisse, M. Mar, L. Frezet, W. Hourani, J.-L. Bubendorff, J. Parmentier, S. Hajjar-Garreau, L. Simon, *Carbon* **2014**, 77, 688.
[114]. D. O'Hagan, *Chem. Soc. Rev.* **2008**, 37, 308.
[115]. N. Watanabe, *Solid State Ion.* **1980**, 1, 87.

[116]. X. Wang, Y. Chen, Y. Dai, Q. Wang, J. Gao, J. Huang, J. Yang, X. Liu, *J. Phys. Chem. C* **2013**, 117, 12078.
[117]. S. Kwon, J.-H. Ko, K.-J. Jeon, Y.-H. Kim, J. Y. Park, *Nano. Lett.* **2012**, 12, 6043.
[118]. G. Zhang, X. Yang, M. Dubois, M. Herraiz, R. Chenitz, M. Lefèvre, M. Cherif, F. Vidal, V. P. Glibin, S. Sun, J.-P. Dodelet, *Energy Environ. Sci.* **2019**, 12, 3015.
[119]. J. H. Sanders, J. N. Cutler, G. John, *Appl. Surf. Sci.* **1998**, 135, 169.
[120]. R. Thorpe, S. Rangan, R. Whitcomb, A. C. Basaran, T. Saerbeck, I. K. Schuller, R. A. Bartynski, *Phys. Chem. Chem. Phys.* **2015**, 17, 15218.
[121]. I. Matanovic, K. Artyushkova, P. Atanassov, *Curr Opin Electrochem.* **2018**, 9, 137.
[122]. M. Panich, A. I. Shames, T. Nakajima, *J. Phys. Chem. Solids* **2001**, 62, 959.
[123]. H. Yokomichi, T. Hayashi, T. Amano, A. Masuda, *J. Non. Cryst. Solids* **1998**, 227-230, 641.
[124]. K. Takai, H. Sato, T. Enoki, N. Yoshida, F. Okino, H. Touhara, M. Endo, *Mol. Cryst. Liq. Cryst.* **2000**, 340, 289.
[125]. V. I. Krinichnyi, H. K. Roth, M. Schrödner, B. Wessling, *Polymer* **2006**, 47, 7460.
[126]. V. Krinichnyi, S. V. Tokarev, H. K. Roth, M. Schrödner, B. Wessling, *Synth. Met.* **2006**, 156, 1368.
[127]. A. Tressaud, F. Moguet, S. Flandrois, M. Chambon, C. Guimon, G. Nanse, E. Papirer, V. Gupta, O. P. Bahl, *J. Phys. Chem. Solids* **1996**, 57, 745.
[128]. J.-C. Agopian, O. Téraube, K. Charlet, S. Hajjar-Garreau, E. Petit, N. Batisse, M. Dubois, *Appl. Surf. Sci.* **2022**, 595, 153561.
[129]. P. F. Fulvio, S. S. Brown, J. Adcock, R. T. Mayes, B. Guo, X.-G. Sun, S. M. Mahurin, G. M. Veith, S. Dai, *Chem. Mater.* **2011**, 23, 4420.
[130]. E. Disa, M. Dubois, K. Guérin, H. Kharbache, F. Masin, A. Hamwi, *Carbon* **2011**, 49, 4801.
[131]. N. Nadiege, E. Disa, P. Thomas, L. Romana, J. L. Mansot, M. Dubois, K. Guérin, W. Zhang, A. Hamwi, *J. Fluor. Chem.* **2012**, 144, 10.
[132]. Y. Ahmad, M. Dubois, K. Guérin, A. Hamwi, Z. Fawal, A. P. Kharitonov, A. V. Generalov, A. Yu. Klyushin, K. A. Simonov, N. A. Vinogradov, I. A. Zhdanov, A. B. Preobrajenski, A. S. Vinogradov, *J. Phys. Chem. C* **2013**, 117, 13564.
[133]. V. Y. Osipov, N. M. Romanov, K. Kogane, H. Touhara, Y. Hattori, K. Takai, *Mendeleev Commun.* **2020**, 30, 84.
[134]. M. Herraiz, N. Batisse, M. Dubois, V. V. Nesvizhevsky, C. Cavallari, M. Brunelli, V. Pischedda, S. Radescu, *J. Phys. Chem. C* **2020**, 124, 14229.
[135]. C. Cavallari, M. Brunelli, S. Radescu, M. Dubois, N. Batisse, G. B. M. Vaughan, H. E. Fischer, V. Pischedda, *Carbon* **2019**, 147, 1.
[136]. K. Yoshida, Y. Sugawara, M. Saitoh, K. Matsumoto, R. Hagiwara, Y. Matsuo, A. Kuwabara, Y. Ukyo, Y. Ikuhara, *J. Power Sources* **2020**, 445, 227320.
[137]. T. Hayashi, M. Terrones, C. Scheu, Y. A. Kim, M. Rühle, T. Nakajima, M. Endo, *Nano Letters* **2002**, 2, 491.
[138]. M. Colin, X. Chen, M. Dubois, A. Rawal, D. J. Kim, *Applied Surface Science* **2022**, 583, 152534.
[139]. H. Sugiyama, Y. Hattori, *Chem. Phys. Lett.* **2020**, 758, 137909.
[140]. L. F. Velasco, K. H. Kim, Y. S. Lee, P. Lodewyckx, *Front. Chem.* **2020**, 8, 593756.
[141]. S. M. Lyth, W. Ma, J. Liu, T. Daio, K. Sasaki, A. Takahara, B. Ameduri, *Nanoscale* **2015**, 7, 16087.
[142]. K. Fan, X. Chen, X. Wang, X. Liu, Y. Liu, W. Lai, X. Liu, *ACS Appl. Mater. Interfaces* **2018**, 10, 28828.
[143]. D. Saurel, J. Segalini, M. Jauregui, A. Pendashteh, B. Daffos, P. Simon, M. Casas-Cabanas, *Energy Storage Mater.* **2019**, 21, 162.

[144]. V. Mazánek, O. Jankovský, J. Luxa, D. Sedmidubský, Z. Janoušek, F. Šembera, M. Mikulics, Z. Sofer, *Nanoscale* **2015**, 7, 13646.
[145]. M. Panich, A. I. Shames, T. Nakajima, *J. Phys. Chem. Solids.* **2001**, 62, 959.
[146]. C. Iojoiu, F. Alloin, J.-Y. Sanchez, *Actualite Chimique* **2006**, 135.
[147]. F. C. Lee, M. S. Ismail, D. B. Ingham, K. J. Hughes, L. Ma, S. M. Lyth, M. Pourkashanian, *Renew. Sustain. Energy Rev.* **2022**, 166, 112640.
[148]. W. E. Mustain, M. Chatenet, M. Page, Y. S. Kim, *Energy Environ. Sci.* **2020**, 13, 2805.
[149]. X. Peng, D. Kulkarni, Y. Huang, T. J. Omasta, B. Ng, Y. Zheng, L. Wang, J. M. LaManna, D. S. Hussey, J. R. Varcoe, I. V. Zenyuk, W. E. Mustain, *Nat. Commun.* **2020**, 11, 3561.
[150]. D. Choi, J.-H. Jang, D. Lee, Y. S. Kang, H. Jin, K.-Y. Lee, S. Yoo, *J. Power Sources* **2021**, 494, 229738.
[151]. J. Hyun, W. Jo, S. H. Yang, S.-H. Shin, G. Doo, S. Choi, D.-H. Lee, D. W. Lee, E. Oh, J. Y. Lee, H.-T. Kim, *J. Power Sources* **2022**, 543, 231835.
[152]. M. Ouattara-Brigaudet, S. Berthon-Fabry, C. Beauger, P. Achard, *Int. J. Hydrog. Energy.* **2014**, 39, 1420.
[153]. B. Chokkiah, S. M. Wabaidur, M. R. Siddiqui, M. A. Islam, R. Dhanusuraman, V. K. Ponnusamy, *Fuel* **2022**, 324, 124496.
[154]. B. Iskandarani, N. Rajabalizadeh Mojarrad, A. Yürüm, S. Alkan Gürsel, B. Yarar Kaplan, *Energ. Fuel* **2022**, 36, 9282.
[155]. A. Liu, W. Li, H. Jin, X. Yu, Y. Bu, Y. He, H. Huang, S. Wang, J. Wang, *Electrochim. Acta* **2015**, 177, 36.
[156]. H. Wang, A. Kong, *Mater. Lett.* **2014**, 136, 384.
[157]. S. Geiger, O. Kasian, A. M. Mingers, K. J. J. Mayrhofer, S. Cherevko, *Sci. Rep.* **2017**, 7, 4595.
[158]. J. M. Kim, Y. J. Lee, S.-h. Kim, K.-H. Chae, K. R. Yoon, K. A. Lee, A. Byeon, Y. S. Kang, H.-Y. Park, M. K. Cho, H. C. Ham, J. Y. Kim, *Nano Energy* **2019**, 65, 104008.
[159]. J. Zhang, F. Coms, S. Kumaraguru, *J. Electrochem. Soc.* **2021**, 168, 024520.
[160]. L. Dubau, F. Maillard, M. Chatenet, S. Cavaliere, I. Jiménez-Morales, A. Mosdale, R. Mosdale, *Energies* **2020**, 13, 403.
[161]. L. Dubau, L. Castanheira, M. Chatenet, F. Maillard, J. Dillet, G. Maranzana, S. Abbou, O. Lottin, G. De Moor, A. El Kaddouri, C. Bas, L. Flandin, E. Rossinot, N. Caqué, *Int. J. Hydrog. Energy* **2014**, 39, 21902.
[162]. L. Dubau, L. Castanheira, F. Maillard, M. Chatenet, O. Lottin, G. Maranzana, J. Dillet, A. Lamibrac, J.-C. Perrin, E. Moukheiber, A. ElKaddouri, G. De Moor, C. Bas, L. Flandin, N. Caqué, *WIREs Energy. Environ.* **2014**, 3, 540.
[163]. A. Zadick, L. Dubau, N. Sergent, G. Berthomé, M. Chatenet, *ACS Catal.* **2015**, 5, 4819.
[164]. C. Lafforgue, A. Zadick, L. Dubau, F. Maillard, M. Chatenet, *Fuel Cells* **2018**, 18, 229.
[165]. C. Lafforgue, F. Maillard, V. Martin, L. Dubau, M. Chatenet, *ACS Catal.* **2019**, 9, 5613.
[166]. Y. Yi, G. Weinberg, M. Prenzel, M. Greiner, S. Heumann, S. Becker, R. Schlögl, *Catal. Today* **2017**, 295, 32.
[167]. L. Castanheira, L. Dubau, M. Mermoux, G. Berthomé, N. Caqué, E. Rossinot, M. Chatenet, F. Maillard, *ACS Catal.* **2014**, 4, 2258.
[168]. L. Castanheira, W. O. Silva, F. H. B. Lima, A. Crisci, L. Dubau, F. Maillard, *ACS Catal.* **2015**, 5, 2184.
[169]. F. Forouzandeh, X. Li, D. W. Banham, F. Feng, A. Joseph Kakanat, S. Ye, V. Birss, *J. Power Sources* **2018**, 378, 732.

[170]. S. Luong, M. Atwa, M. O. Valappil, V. I. Birss, *J. Electrochem. Soc.* **2022**, 169, 031512.
[171]. M. N. Islam, U. Shrivastava, M. Atwa, X. Li, V. Birss, K. Karan, *ACS Appl. Mater. Interfaces* **2020**, 12, 39215.
[172]. S. G. Peera, A. Arunchander, A. K. Sahu, *Carbon* **2016**, 107, 667.
[173]. S. Akula, P. Varathan, A. Kesh, K. Tammeveski, G. Peera, S. Panda, B. Balasubramaniam, A. K. Sahu, *Int. J. Hydrog. Energy* **2022**, 47, 20617.
[174]. Y.-B. Park, E. You, C. Pak, M. Min, *Electrochim. Acta* **2018**, 284, 242.
[175]. J. L. Bott-Neto, T. Asset, F. Maillard, L. Dubau, Y. Ahmad, K. Guérin, S. Berthon-Fabry, A. Mosdale, R. Mosdale, E. A. Ticianelli, M. Chatenet, *J. Power Sources* **2018**, 404, 28.
[176]. S. Jin, S. Y. Yang, J. M. Lee, M. S. Kang, S. M. Choi, W. Ahn, X. Fuku, R. M. Modibedi, B. Han, M. H. Seo, *ACS Appl. Mater. Interfaces* **2021**, 13, 26936.
[177]. L. Qu, Y. Liu, J.-B. Baek, L. Dai, *ACS Nano* **2010**, 4, 1321.
[178]. L. Dai, Y. Xue, L. Qu, H.-J. Choi, J.-B. Baek, *Chem. Rev.* **2015**, 115, 4823.
[179]. M. Shao, Q. Chang, J. P. Dodelet, R. Chenitz, *Chem. Rev.* **2016**, 116, 3594.
[180]. G. Wu, K. L. More, C. M. Johnston, P. Zelenay, *Science (New York, N.Y.)* **2011**, 332, 443.
[181]. X. Yang, Y. Wang, G. Zhang, L. Du, L. Yang, M. Markiewicz, J.-y. Choi, R. Chenitz, S. Sun, *Appl. Catal. B.* **2020**, 264, 118523.
[182]. J. Zhao, C. R. Cabrera, Z. Xia, Z. Chen, *Carbon* **2016**, 104, 56.
[183]. K. Kakaei, A. Balavandi, *J. Colloid Interface Sci.* **2016**, 463, 46.
[184]. T. V. Vineesh, M. A. Nazrulla, S. Krishnamoorthy, T. N. Narayanan, S. Alwarappan, *Appl. Mater. Today.* **2015**, 1, 74.
[185]. H. Peng, F. Liu, X. Qiao, Z. Xiong, X. Li, T. Shu, S. Liao, *Electrochim. Acta* **2015**, 182, 963.
[186]. X. Sun, P. Song, Y. Zhang, C. Liu, W. Xu, W. Xing, *Sci. Rep.* **2013**, 3, 2505.
[187]. H.-J. Zhang, X. Zhang, S. Yao, H. Hu, Z.-F. Ma, J. Yang, *J. Electrochem. Soc.* **2017**, 164, H1081.
[188]. X. Qiao, S. Liao, G. Wang, R. Zheng, H. Song, X. Li, *Carbon* **2016**, 99, 272.
[189]. S. Jiang, Y. Sun, H. Dai, J. Hu, P. Ni, Y. Wang, Z. Li, Z. Li, *Nanoscale* **2015**, 7, 10584.
[190]. R. Baker, D. P. Wilkinson, J. Zhang, *Electrochim. Acta* **2008**, 53, 6906.
[191]. V. G. Khomenko, V. Z. Barsukov, A. S. Katashinskii, *Electrochim. Acta* **2005**, 50, 1675.
[192]. H. Behret, H. Binder, G. Sandstede, *Electrochim. Acta* **1975**, 20, 111.
[193]. A. Ishihara, Y. Ohgi, K. Matsuzawa, S. Mitsushima, K.-i. Ota, *Electrochim. Acta* **2010**, 55, 8005.
[194]. M. S. Thorum, J. Yadav, A. A. Gewirth, *Angew. Chem. Int. Ed.* **2009**, 48, 165.
[195]. Y.-C. Wang, P.-F. Zhu, H. Yang, L. Huang, Q.-H. Wu, M. Rauf, J.-Y. Zhang, J. Dong, K. Wang, Z.-Y. Zhou, S.-G. Sun, *ChemElectroChem* **2018**, 5, 1914.
[196]. M. Cherif, J.-P. Dodelet, G. Zhang, V. P. Glibin, S. Sun, F. Vidal, *Molecules* **2021**, 26, 7370.
[197]. V. P. Glibin, M. Cherif, F. Vidal, J.-P. Dodelet, G. Zhang, S. Sun, *J. Electrochem. Soc.* **2019**, 166, F3277.